

<sup>1</sup> **Highlights**

<sup>2</sup> **Oscillatory instabilities in dynamically active signalling compartments coupled via bulk diffusion in a 3-D**  
<sup>3</sup> **spherical domain**

<sup>4</sup> Sarafa Iyaniwura, Michael J. Ward

<sup>5</sup> • Derivation of an ODE system for a cell-bulk ODE-  
<sup>6</sup> PDE model in a bounded 3-D domain in the near  
<sup>7</sup> well-mixed limit. The effect of spatial inhomogeneities  
<sup>8</sup> in the cell population is incorporated by  
<sup>9</sup> the Neumann Green's matrix, and there is a diffu-  
<sup>10</sup> sion parameter.

<sup>11</sup> • Hopf bifurcations in the ODE system trigger intra-  
<sup>12</sup> cellular oscillations as predicted by global bifur-  
<sup>13</sup> cation diagrams computed with MATCONT. Syn-  
<sup>14</sup> chronization is studied via the Kuramoto order pa-  
<sup>15</sup> rameter.

<sup>16</sup> • Quorum-sensing collective dynamics are illus-  
<sup>17</sup> trated as the number of cells exceeds a threshold.  
<sup>18</sup> Diffusion-mediated intracellular communication is  
<sup>19</sup> also illustrated.

<sup>20</sup> • In the non well-mixed limit, where spatial effects  
<sup>21</sup> are important, a novel integro-differential system  
<sup>22</sup> is derived to characterize intracellular oscillations.

# Oscillatory instabilities in dynamically active signalling compartments coupled via bulk diffusion in a 3-D spherical domain

Sarafa Iyaniwura<sup>a</sup>, Michael J. Ward<sup>b</sup>

<sup>a</sup>Theoretical Biology and Biophysics, Theoretical Division, Los Alamos National Laboratory, Los Alamos, NM, 87545, USA

<sup>b</sup>Dept. of Mathematics, University of British Columbia, Vancouver, B.C., Canada, V6T 1Z2 (corresponding author)

---

## Abstract

For a coupled cell-bulk ODE-PDE model in a three-dimensional spherical domain, we analyze oscillatory dynamics in spatially segregated dynamically active signalling compartments that are coupled through a passive extracellular bulk diffusion field. Within the confining spherical domain, the signalling compartments are a collection of small spheres of a common radius  $O(\varepsilon) \ll 1$ . In our cell-bulk model, each cell secretes a signalling chemical into the extracellular bulk region, while also receiving a chemical feedback that is produced by all the other cells. This secretion and global feedback of chemical into the cells is regulated by permeability parameters on the cell membrane. In the near well-mixed limit corresponding to a large bulk diffusivity  $D = D_0/\varepsilon \gg 1$ , where  $D_0 = O(1)$ , the method of matched asymptotic expansions is used to reduce the cell-bulk model to a novel nonlinear ODE system for the intracellular concentrations and the spatially averaged bulk diffusion field. The novelty in this ODE system, as compared to the type of ODE system that typically is studied in the well-mixed limit, is that it involves  $D_0$  and an  $O(\varepsilon)$  correction term that incorporates the spatial configuration of the signalling compartments. For the case of Sel'kov intracellular kinetics, this new ODE system is used to study Hopf bifurcations that are triggered by the global coupling. In addition, the Kuramoto order parameter is used to study phase synchronization for the leading-order ODE system. The spatial configuration of cells is also shown to influence both quorum-sensing behavior and diffusion-mediated communication that lead to synchronous intracellular oscillations. Finally, for the non well-mixed regime where  $D = O(1)$ , we use asymptotic analysis in the limit  $\varepsilon \rightarrow 0$  to derive a new integro-differential ODE system for the intracellular dynamics.

**Keywords:** Bulk diffusion, Green's function, synchronous oscillations, Kuramoto order parameter, Hopf bifurcation, quorum-sensing, strong localized perturbation theory, integro-differential systems.

---

23    **1. Introduction**

24    Bacteria and other microorganisms communicate and  
25    coordinate their activities in order to accomplish tasks  
26    that cannot be achieved by a single cell. Cells that are  
27    not in close proximity communicate via their extracel-  
28    lular environment through both the secretion of a sig-  
29    nalling chemical into the extracellular medium and the  
30    absorption of the global concentration field that is pro-  
31    duced by all the other cells. This feedback enables the  
32    cells to adjust their intracellular dynamics accordingly.  
33    Examples of biological systems that exhibit this kind of  
34    communication include a colony of starving yeast cells  
35    in which the exchange of acetaldehyde (Ace) molecules  
36    leads to glycolytic oscillations (cf. [1, 2, 3]), a col-  
37    lection of social amoebae *Dictyostelium discoideum*,  
38    where the secretion of cyclic adenosine monophosphate  
39    (cAMP) by the cells leads to synchronous oscillation in

40    their intracellular dynamics and guides them to aggrega-  
41    tion (cf. [4, 5, 6]), and a colony of the marine bacterium  
42    *Vibrio fischeri* that leads to bioluminescence in certain  
43    species of tropical squid (cf. [7, 8]).

44    This type of intracellular communication through a bulk  
45    diffusion field is closely associated with *quorum sens-  
46    ing (QS)*, a phenomenon by which the onset of collec-  
47    tive intracellular dynamics occurs when the cell den-  
48    sity increases past a threshold. Mathematical models of  
49    quorum-sensing usually focus on the well-mixed limit  
50    where the bulk diffusion field is spatially uniform. In  
51    other non well-mixed situations where spatial effects  
52    are important, the bulk diffusivity and bulk degrada-  
53    tion control the onset of collective intracellular dynam-  
54    ics through spatial gradients, a phenomenon referred to  
55    as *diffusion sensing (DS)* or *diffusion-mediated synchro-  
56    nization*. QS systems are categorized into two main

groups. The first group includes yeast cells and social amoeba, where a switch-like transition leads to synchronous oscillations as the cell population density passes a threshold (cf. [4, 9, 10, 3, 2, 1]). Physiochemical systems involving groups of catalyst-loaded small particles immersed in a Belousov-Zhabotinsky reaction mixture are also known to exhibit collective chemical oscillations (cf. [11, 12, 13, 14]). The second group of QS system includes a colony of the marine bacterium *Vibrio fischeri* and the human pathogen *Pseudomonas aeruginosa*, where a sudden transition between bistable steady-states occurs as the cell population density exceeds a certain threshold (cf. [15, 16, 8, 17]).

Various mathematical modeling frameworks have been developed to study the mechanism through which communication is achieved between spatially segregated active cells [18, 19, 20, 21, 22]. In this paper, we extend the coupled 2-D cell-bulk ODE-PDE model of [18, 23, 24] to a 3-D spherical domain, where the cells are small spheres of a common radius within the domain (see Fig. 1). Our model is inspired by the 3-D cell-bulk model formulated in [19, 20, 25] in all of  $\mathbb{R}^3$ , where there was a single intracellular species within each cell and where the bulk medium was purely diffusive. By allowing for multi-component intracellular species in a finite 3-D domain, and including both bulk diffusion and bulk degradation, we will show that our extended cell-bulk model can lead to synchronous intracellular oscillations. In our model, the secretion of a signalling molecule and the global feedback from the bulk medium are regulated by permeability parameters on the cell membrane, while spatio-temporal bulk diffusion fields in the extracellular medium are modeled explicitly with a PDE. This latter feature is in contrast to the approach in [22] where heterogeneity in the extracellular medium was modeled with a discrete diffusion equation, and in [21] where the signalling compartments were globally coupled through an ODE. Our main goal is to use the 3-D cell-bulk model to study the emergence and synchronization of intracellular oscillations that is mediated by the bulk diffusion field. We also investigate mechanisms that promote either quorum sensing or diffusion-mediated synchronization.

The formulation of our coupled ODE-PDE model is as follows. Let  $\Omega \subset \mathbb{R}^3$  be a bounded spherical domain of radius  $L$  containing  $m$  signalling compartments, denoted by  $\Omega_j$  for  $j = 1, \dots, m$ , which are smaller spheres of radius  $R$ , centered at  $\mathbf{X}_j \in \Omega$  for  $j = 1, \dots, m$ . In the bulk region  $\Omega \setminus \cup_{j=1}^m \Omega_j$  and for  $T > 0$ , the concentration  $\mathcal{U}(\mathbf{X}, T)$  of the bulk signalling species or autoinducer

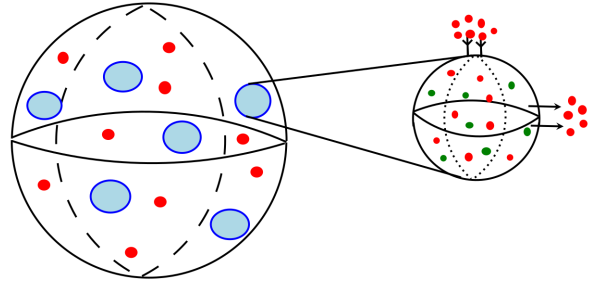


Figure 1: A schematic diagram showing dynamically active signalling compartments (in blue) in a 3-D spherical domain. Each signalling compartment is a smaller sphere containing two chemical species represented by green and red dots, where only the red chemical is secreted into the extracellular bulk region. Right panel: Zoomed-in illustration of the intracellular concentration of chemicals within each signalling compartment, the secretion of signalling molecules into the bulk region, and the feedback of chemical into the cells.

satisfies

$$\mathcal{U}_T = D_B \Delta \mathcal{U} - k_B \mathcal{U}, \quad \mathbf{X} \in \Omega \setminus \cup_{j=1}^m \Omega_j, \quad (1.1a)$$

$$\partial_{n_X} \mathcal{U} = 0, \quad \mathbf{X} \in \partial \Omega, \quad (1.1b)$$

$$D_B \partial_{n_X} \mathcal{U} = \beta_{1j} \mathcal{U} - \beta_{2j} \mu_j^1, \quad \mathbf{X} \in \partial \Omega_j, \quad j = 1, \dots, m, \quad (1.1c)$$

where  $D_B > 0$  and  $k_B > 0$  are the dimensional diffusivity and decay rate of the bulk species, respectively,  $\beta_{1j} > 0$  and  $\beta_{2j} > 0$  are the dimensional rate of influx and efflux of chemical into and out of the  $j^{\text{th}}$  cell, respectively, and  $\partial_{n_X}$  denotes the outer normal derivative on  $\Omega$ , which points into the bulk region. We assume that there are  $n$  interacting non-diffusing species within each cell represented by the vector  $\mu_j \equiv (\mu_j^1, \dots, \mu_j^n)^T$  for the  $j^{\text{th}}$  cell. Since the intracellular environment is assumed to be well-mixed, the  $n$  species are assumed to interact according to the local reaction-kinetics  $\mathbf{F}_j(\mu/\mu_c)$ . For each  $j = 1, \dots, m$ , the intracellular dynamics within the  $j^{\text{th}}$  cell is coupled to the extracellular bulk diffusion field in (1.1) through the integration of the diffusive flux across the membrane of the cell as

$$\frac{d\mu_j}{dT} = k_R \mu_c \mathbf{F}_j \left( \mu_j / \mu_c \right) + \mathbf{e}_1 \int_{\partial \Omega_j} \left( \beta_{1j} \mathcal{U} - \beta_{2j} \mu_j^1 \right) dS_X. \quad (1.1d)$$

Here  $\mathbf{e}_1 \equiv (1, 0, \dots, 0)^T$ ,  $k_R > 0$  is the reaction rate for the dimensionless local reaction kinetics  $\mathbf{F}_j$ , and  $\mu_c > 0$  is a typical value for  $\mu_j$ . Each cell secretes only one signalling chemical, labeled by  $\mu_j^1$ , into the bulk medium as regulated by the efflux permeability parameter  $\beta_{2j}$ . The global feedback into the  $j^{\text{th}}$  cell, which is produced by the entire cell population, is regulated by the influx permeability parameter  $\beta_{1j}$ . A schematic illustration of the

<sup>109</sup> cell-bulk coupling in (1.1) is shown in Fig. 1 for  $m = 6$   
<sup>110</sup> cells, each with  $n = 2$  intracellular species.

For our asymptotic limit, we assume that the common radius  $R$  of the signalling compartments  $\Omega_j$  for  $j = 1, \dots, m$  is small relative to the radius  $L$  of the spherical domain  $\Omega$ . As such, we introduce a small scaling parameter  $\varepsilon \equiv R/L \ll 1$ . By non-dimensionalizing the coupled ODE-PDE model (1.1) as in Appendix A, we obtain that the dimensionless concentration  $U(\mathbf{x}, t)$  in the bulk region satisfies for  $t > 0$

$$\frac{\partial U}{\partial t} = D\Delta U - \kappa U, \quad \mathbf{x} \in \Omega \setminus \cup_{j=1}^m \Omega_{\varepsilon_j}, \quad (1.2a)$$

$$\partial_n U = 0, \quad \mathbf{x} \in \partial\Omega, \quad (1.2b)$$

$$\varepsilon D \partial_n U = d_{1j} U - \frac{d_{2j}}{\varepsilon} u_j^1, \quad \mathbf{x} \in \partial\Omega_{\varepsilon_j}, \quad j = 1, \dots, m, \quad (1.2c)$$

which is coupled to the dimensionless intracellular dynamics within the  $j^{\text{th}}$  cell, for each  $j = 1, \dots, m$ , by

$$\frac{d\mathbf{u}_j}{dt} = \mathbf{F}_j(\mathbf{u}_j) + \frac{\mathbf{e}_1}{\varepsilon^2} \int_{\partial\Omega_{\varepsilon_j}} (\varepsilon d_{1j} U - d_{2j} u_j^1) dS_{\mathbf{x}}. \quad (1.2d)$$

Here  $\mathbf{u}_j \equiv (u_j^1, \dots, u_j^n)^T$  is a vector representing the dimensionless molar concentration of the  $n$  species in the  $j^{\text{th}}$  cell, labeled by  $\Omega_{\varepsilon_j} \equiv \{\mathbf{x} | |\mathbf{x} - \mathbf{x}_j| \leq \varepsilon\}$ . We assume that the cells are *well-separated* in the sense that  $\text{dist}(\mathbf{x}_j, \mathbf{x}_k) = O(1)$  for  $j \neq k$  and  $\text{dist}(\mathbf{x}_j, \partial\Omega) = O(1)$  as  $\varepsilon \rightarrow 0$ . The key  $O(1)$  parameters in the dimensionless cell-bulk model (1.2) are

$$D \equiv \frac{D_B}{k_R L^2}, \quad \kappa \equiv \frac{k_B}{k_R}, \quad (1.3)$$

$$d_{1j} \equiv \varepsilon \frac{\beta_{1j}}{k_R L}, \quad d_{2j} \equiv \varepsilon^2 \frac{\beta_{2j} L^2}{k_R}. \quad (1.3)$$

<sup>111</sup> Here  $D$  and  $\kappa$  are the effective diffusion coefficient and  
<sup>112</sup> bulk decay rate of the bulk species, respectively. The  
<sup>113</sup> scaling limit chosen for the permeability parameters is  
<sup>114</sup> necessary to compensate for the small size of the cells  
<sup>115</sup> relative to the volume of the domain, and the rapid de-  
<sup>116</sup> cay of the 3-D free-space Green's function (see Ap-  
<sup>117</sup> pendix A). Since the bulk decay rate  $\kappa$  is the ratio of the  
<sup>118</sup> dimensional bulk decay rate to the reaction rate of the  
<sup>119</sup> intracellular kinetics, an increase in  $\kappa$  corresponds to an  
<sup>120</sup> increase in the rate of degradation of the bulk species  
<sup>121</sup> relative to the rate they are produced within the cells.  
<sup>122</sup> In particular for large  $\kappa$ , the chemical signal secreted by  
<sup>123</sup> the cells decays on a short length-scale, resulting in a  
<sup>124</sup> rather weak coupling between the cells. In terms of the  
<sup>125</sup> effective bulk diffusivity  $D$ , for large values of  $D$  relative  
<sup>126</sup> to  $\kappa$ , the spatial gradients in the bulk medium are

<sup>127</sup> weak and there is effectively a global coupling between  
<sup>128</sup> the cells.

The outline of the paper is as follows. In the *near well-mixed limit* corresponding to a large bulk diffusivity  $D = D_0/\varepsilon \gg 1$ , with  $D_0 = O(1)$ , in §2 the method of matched asymptotic expansions is used to derive a novel ODE system from the cell-bulk model (1.2). The novelty in this ODE system is that it involves  $D_0$  and includes an  $O(\varepsilon)$  correction term that accounts for the spatial configuration of the small cells. For the special case of Sel'kov intracellular kinetics, in §3 the leading-order dynamics of this ODE system is analyzed to predict Hopf bifurcations that initiate intracellular oscillations. Quorum-sensing and phase synchronization of large amplitude intracellular oscillations, as based on the Kuramoto order parameter, are also studied for a heterogeneous population of cells. In §4, we study the effect of the spatial configuration of cells on intracellular dynamics by considering three distinct configurations of cells in the unit sphere: cells whose centers are symmetrically located on a concentric spherical ring within the sphere, cells whose centers are arbitrarily located on the concentric ring within the sphere, and cells that are arbitrarily located within the sphere. The Kuramoto order parameter is computed to show that diffusion-mediated synchronization can be achieved as  $D_0$  is increased, even when the cells are arbitrarily located in the sphere. For each of the spatial configurations of cells in §4, in §5 we illustrate QS behavior by showing that a single *defective* or *pacemaker* cell can trigger synchronous intracellular dynamics in the entire cell population, which otherwise would not exhibit oscillatory dynamics. In §6 we derive a new integro-differential ODE system for intracellular dynamics for the non-well mixed case where  $D = O(1)$ . Finally, in §7 we briefly summarize our results and discuss a few open directions.

## 2. Asymptotics of the cell-bulk model for large $D$

In the limit  $\varepsilon \rightarrow 0$ , we use strong localized perturbation theory [26] to analyze (1.2) in the regime of a fast diffusing bulk species and a large rate of global feedback into the cells. Our goal is to derive an ODE system that has a diffusion parameter and also a weak perturbation term that incorporates the spatial configuration of cells.

We begin our analysis by rescaling the effective bulk diffusivity  $D$  and the influx permeability  $d_{1j}$  as

$$D = \frac{D_0}{\varepsilon} \quad \text{and} \quad d_{1j} = \frac{\tilde{d}_{1j}}{\varepsilon}, \quad j = 1, \dots, m, \quad (2.1)$$

where  $D_0 \equiv O(1)$  and  $\tilde{d}_{1j} \equiv O(1)$ . With this scaling, dimensionless bulk concentration for  $t > 0$  satisfies

$$\frac{\partial U}{\partial t} = \frac{D_0}{\varepsilon} \Delta U - \kappa U, \quad \mathbf{x} \in \Omega \setminus \cup_{j=1}^m \Omega_{\varepsilon_j}, \quad (2.2a)$$

$$\partial_n U = 0, \quad \mathbf{x} \in \partial\Omega, \quad (2.2b)$$

$$\varepsilon D_0 \partial_n U = \tilde{d}_{1j} U - d_{2j} u_j^1, \quad \mathbf{x} \in \partial\Omega_{\varepsilon_j}, \quad j = 1, \dots, m, \quad (2.2c)$$

which is coupled to the dynamics within the  $j^{\text{th}}$  cell by

$$\frac{d\mathbf{u}_j}{dt} = \mathbf{F}_j(\mathbf{u}_j) + \frac{\mathbf{e}_1}{\varepsilon^2} \int_{\partial\Omega_{\varepsilon_j}} (\tilde{d}_{1j} U - d_{2j} u_j^1) dS_{\mathbf{x}}, \quad (2.2d)$$

<sup>170</sup> for  $j = 1, \dots, m$ .

For  $D = D_0/\varepsilon \gg O(1)$ , we expand  $U(\mathbf{x}, t)$  in the outer region at  $O(1)$  distances from the cells as

$$U(\mathbf{x}, t) = U_0(\mathbf{x}, t) + \frac{\varepsilon}{D_0} U_1(\mathbf{x}, t) + \dots \quad (2.3)$$

Upon substituting (2.3) into (2.2) and collecting terms in powers of  $\varepsilon$ , we obtain the leading-order problem

$$\Delta U_0 = 0, \quad \mathbf{x} \in \Omega; \quad \partial_n U_0 = 0, \quad \mathbf{x} \in \partial\Omega, \quad (2.4)$$

for which  $U_0 \equiv U_0(t)$  is the solution. The next-order problem for  $U_1$  in the outer region is

$$\begin{aligned} \Delta U_1 &= U'_0 + \kappa U_0, \quad \mathbf{x} \in \Omega \setminus \{\mathbf{x}_1, \dots, \mathbf{x}_m\}, \\ \partial_n U_1 &= 0, \quad \mathbf{x} \in \partial\Omega, \end{aligned} \quad (2.5)$$

<sup>171</sup> where we must determine the appropriate singularity behavior of  $U_1$  as  $\mathbf{x} \rightarrow \mathbf{x}_j$  for each  $j = 1, \dots, m$ .

In the inner region, defined at an  $O(\varepsilon)$  neighborhood of the  $j^{\text{th}}$  cell, we introduce the inner variables  $\mathbf{y} = \varepsilon^{-1}(\mathbf{x} - \mathbf{x}_j)$  and  $U(\mathbf{x}, t) = V_j(\mathbf{x}_j + \varepsilon\mathbf{y}, t)$ , with  $\rho = |\mathbf{y}|$ . Upon writing (2.2a) and (2.2c) in terms of the inner variables, we obtain for each  $j = 1, \dots, m$  that as  $\varepsilon \rightarrow 0$ ,

$$\begin{aligned} \Delta_\rho V_j &= 0, \quad \rho > 1; \quad V_j \rightarrow v_{j\infty} \quad \text{as} \quad \rho \rightarrow \infty, \\ D_0 \partial_\rho V_j &= \tilde{d}_{1j} V_j - d_{2j} u_j^1, \quad \text{on} \quad \rho = 1, \end{aligned} \quad (2.6)$$

<sup>172</sup> where  $\Delta_\rho \equiv \partial_{\rho\rho} + 2\rho^{-1}\partial_\rho$ , and  $v_{j\infty}$  is the constant far-field behaviour, which may depend on  $\varepsilon$ . The solution to (2.6) is

$$V_j = \frac{c_j}{\rho} + v_{j\infty} \quad \text{where} \quad c_j = \frac{d_{2j} u_j^1 - \tilde{d}_{1j} v_{j\infty}}{\tilde{d}_{1j} + D_0}. \quad (2.7)$$

Upon matching the inner solution (2.7) to the outer expansion in (2.3), we obtain a singularity behavior for  $U_1$

as  $\mathbf{x} \rightarrow \mathbf{x}_j$ . In terms of a delta distribution, the singularity behavior for  $U_1$  is combined with (2.5) to derive the complete outer problem for  $U_1$  given by

$$\begin{aligned} \Delta U_1 &= U'_0 + \kappa U_0 - 4\pi D_0 \sum_{i=1}^m c_i \delta(\mathbf{x} - \mathbf{x}_i), \quad \mathbf{x} \in \Omega, \\ \partial_n U_1 &= 0, \quad \mathbf{x} \in \partial\Omega; \quad \int_{\Omega} U_1 d\mathbf{x} = 0, \end{aligned} \quad (2.8)$$

where  $c_i$  is as defined in (2.7) and  $\delta(\mathbf{x} - \mathbf{x}_i)$  is the Dirac delta function localized at the center of the  $i^{\text{th}}$  cell. Without loss of generality, we impose  $\int_{\Omega} U_1 d\mathbf{x} = 0$ , so that the spatial average of  $U$  in the bulk region is  $U_0$ , i.e.  $U_0 = (1/|\Omega|) \int_{\Omega} U d\mathbf{x}$ . By using the divergence theorem, the solvability condition for (2.8) yields the ODE

$$U'_0 + \kappa U_0 = \frac{4\pi D_0}{|\Omega|} \sum_{i=1}^m c_i, \quad (2.9)$$

where  $|\Omega|$  is the domain volume. When this solvability condition holds, we write the solution to (2.8) in terms of the Neumann Green's function  $G(\mathbf{x}; \mathbf{x}_j)$  satisfying

$$\Delta G = \frac{1}{|\Omega|} - \delta(\mathbf{x} - \mathbf{x}_j) \quad \mathbf{x} \in \Omega, \quad (2.10a)$$

$$G(\mathbf{x}; \mathbf{x}_j) \sim \frac{1}{4\pi|\mathbf{x} - \mathbf{x}_j|} + R_j, \quad \text{as} \quad \mathbf{x} \rightarrow \mathbf{x}_j, \quad (2.10b)$$

$$\partial_n G = 0, \quad \mathbf{x} \in \partial\Omega; \quad \int_{\Omega} G d\mathbf{x} = 0, \quad (2.10c)$$

where  $R_j \equiv R(\mathbf{x}_j)$  is its regular part at  $\mathbf{x} = \mathbf{x}_j$ . The solution to the outer problem (2.8) is simply

$$U_1 = 4\pi D_0 \sum_{i=1}^m c_i G(\mathbf{x}; \mathbf{x}_i). \quad (2.11)$$

Expanding (2.11) as  $\mathbf{x} \rightarrow \mathbf{x}_j$  and using the singularity behaviour of the Neumann Green's function given in (2.10b), we obtain for each  $j = 1, \dots, m$  that

$$U_1 \sim \frac{D_0 c_j}{|\mathbf{x} - \mathbf{x}_i|} + 4\pi D_0 (\mathcal{G}\mathbf{c})_j + o(1), \quad \text{as} \quad \mathbf{x} \rightarrow \mathbf{x}_j, \quad (2.12)$$

where  $\mathbf{c} = (c_1, \dots, c_m)^T$  and  $\mathcal{G}$  is the symmetric Neumann Green's matrix whose entries are defined by

$$(\mathcal{G})_{ij} = (\mathcal{G})_{ji} = G(\mathbf{x}_i, \mathbf{x}_j), \quad i \neq j; \quad (\mathcal{G})_{jj} = R_j \equiv R(\mathbf{x}_j). \quad (2.13)$$

Upon substituting (2.12) into the outer expansion in (2.3) and matching the resulting expansion to the far-field behavior of the inner solution (2.7), we obtain as

$\mathbf{x} \rightarrow \mathbf{x}_j$  that

$$v_{j\infty} + \frac{\varepsilon c_j}{|\mathbf{x} - \mathbf{x}_i|} \sim U_0 + \frac{\varepsilon c_j}{|\mathbf{x} - \mathbf{x}_i|} + 4\pi\varepsilon(\mathcal{G}\mathbf{c})_j + o(1). \quad (2.14)$$

From (2.14), we derive the matching condition

$$v_{j\infty} = U_0 + 4\pi\varepsilon(\mathcal{G}\mathbf{c})_j \quad \text{where} \quad c_j = \frac{d_{2j}u_j^1 - \tilde{d}_{1j}v_{j\infty}}{\tilde{d}_{1j} + D_0}, \quad (2.15)$$

for each  $j = 1, \dots, m$ . Observe that the two equations in (2.15) are coupled, since  $c_j$  also depends on  $v_{j\infty}$ . We solve these equations recursively for  $\varepsilon \rightarrow 0$  to obtain

$$v_{j\infty} = U_0 + 4\pi\varepsilon(\mathcal{G}\tilde{\mathbf{c}})_j + O(\varepsilon^2), \quad (2.16a)$$

$$c_j = \tilde{c}_j - \frac{4\pi\varepsilon(\mathcal{G}\tilde{\mathbf{c}})_j \tilde{d}_{1j}}{\tilde{d}_{1j} + D_0} + O(\varepsilon^2), \quad (2.16b)$$

where

$$\tilde{c}_j \equiv \frac{d_{2j}u_j^1 - \tilde{d}_{1j}U_0}{\tilde{d}_{1j} + D_0}, \quad j = 1, \dots, m. \quad (2.16c)$$

Next, we return to the intracellular dynamics of the cells given in (2.2d). Upon evaluating the integral in (2.2d) over the boundary of the  $j^{\text{th}}$  cell, we obtain

$$\frac{d\mathbf{u}_j}{dt} = \mathbf{F}_j(\mathbf{u}_j) - 4\pi D_0 \mathbf{e}_1 c_j, \quad j = 1, \dots, m. \quad (2.17)$$

In deriving (2.17), we used  $\partial_n U|_{\partial\Omega_{\varepsilon_j}} = -D_0 \partial_\rho V_j|_{\rho=1} = -c_j$  on the boundary of the  $j^{\text{th}}$  cell. Upon substituting  $c_j$  as given in (2.16) into (2.9) and (2.17), we obtain an ODE for the spatially averaged bulk species  $U_0$ , which is coupled to an ODE system for the intracellular dynamics. In this way, we obtain the  $nm + 1$  dimensional coupled ODE system

$$U'_0 = -\kappa U_0 + \frac{1}{|\Omega|} \sum_{j=1}^m (k_{2j}u_j^1 - k_{1j}U_0) - \frac{4\pi\varepsilon}{|\Omega|} \sum_{j=1}^m k_{1j}(\mathcal{G}\tilde{\mathbf{c}})_j, \quad (2.18a)$$

$$\frac{d\mathbf{u}_j}{dt} = \mathbf{F}_j(\mathbf{u}_j) - \mathbf{e}_1(k_{2j}u_j^1 - k_{1j}U_0) + 4\pi\mathbf{e}_1\varepsilon k_{1j}(\mathcal{G}\tilde{\mathbf{c}})_j, \quad j = 1, \dots, m, \quad (2.18b)$$

where

$$k_{1j} \equiv \frac{4\pi D_0 \tilde{d}_{1j}}{\tilde{d}_{1j} + D_0}, \quad k_{2j} \equiv \frac{4\pi D_0 d_{2j}}{\tilde{d}_{1j} + D_0}, \\ \tilde{c}_j \equiv \frac{d_{2j}u_j^1 - \tilde{d}_{1j}U_0}{\tilde{d}_{1j} + D_0}, \quad \tilde{\mathbf{c}} \equiv (\tilde{c}_1, \dots, \tilde{c}_m)^T. \quad (2.18c)$$

Here  $\mathcal{G}$  is the Neumann Green's matrix, which depends on the shape of the domain  $\Omega$  and the cell locations  $\mathbf{x}_1, \dots, \mathbf{x}_m$ . Since the novel ODE system (2.18) contains  $D_0$  and a correction term that incorporates the spatial configuration of the cells through the  $\mathcal{G}$  matrix, it can be used to study both quorum and diffusion sensing. Moreover, since the coefficients of the correction terms in (2.18a) and (2.18b) are rather significant for moderately small values of  $\varepsilon$ , we expect that the spatial configuration  $\mathbf{x}_1, \dots, \mathbf{x}_m$  of the cells can influence whether or not intracellular oscillations are triggered.

### 3. Analysis of the leading-order dynamics

In this section, we first perform a Hopf bifurcation analysis on the leading-order dynamics of the ODE system (2.18) (when  $\varepsilon = 0$ ) for identical cells in order to investigate the onset of intracellular oscillations that is triggered by the global coupling. This analysis is done for the two-component kinetics used in [27] to model chemical oscillations, which is a modification of the Sel'kov kinetics [28] used to model glycolysis oscillations. In addition, for this choice of kinetics, quorum sensing and phase synchronization in the intracellular dynamics for the leading-order dynamics is studied using the Kuramoto order parameter (cf. [22, 21, 24]).

#### 3.1. Hopf bifurcation analysis for identical cells

We consider (2.18) in a spherical domain when  $\varepsilon = 0$ . In terms of a cell density parameter defined by  $\rho \equiv m/|\Omega|$ , which measures the number of cells per unit volume, the leading-order ODE system in (2.18) becomes

$$U'_0 = -\kappa U_0 - \frac{\rho}{m} \sum_{j=1}^m (k_{1j}U_0 - k_{2j}u_j^1), \\ \frac{d\mathbf{u}_j}{dt} = \mathbf{F}_j(\mathbf{u}_j) + \mathbf{e}_1(k_{1j}U_0 - k_{2j}u_j^1), \quad j = 1, \dots, m, \quad (3.1a)$$

where  $k_{1j}$  and  $k_{2j}$  are defined in (2.18c).

For identical cells, where the permeabilities and the reaction-kinetics are the same we have  $k_{1j} = k_1$ ,  $k_{2j} = k_2$ , and  $\mathbf{F}(\mathbf{u}) \equiv \mathbf{F}_j(\mathbf{u}_j)$ , with  $\mathbf{u} \equiv \mathbf{u}_j$ , for  $j = 1, \dots, m$ . For this identical cell case, (3.1) reduces to

$$U'_0 = -\kappa U_0 - \rho(k_1 U_0 - k_2 u^1), \\ \frac{d\mathbf{u}}{dt} = \mathbf{F}(\mathbf{u}) + \mathbf{e}_1(k_1 U_0 - k_2 u^1). \quad (3.2)$$

For the reaction kinetics in [27], which we refer to as Sel'kov kinetics, we have  $\mathbf{F} \equiv (f(v, w), g(v, w))^T$ , with

$\mathbf{u} = (u^1, u^2)^T \equiv (v, w)^T$ , where

$$f = \alpha w + wv^2 - v, \quad g = \epsilon_0 [\mu - (\alpha w + wv^2)]. \quad (3.3)$$

The reaction-kinetic parameters  $\alpha$ ,  $\mu$ , and  $\epsilon_0$  are all positive. Upon substituting (3.3) into (3.2), the steady-state solution for (3.2) is

$$\begin{aligned} u_e^1 &= \frac{\mu(\kappa + k_1\rho)}{(\kappa + \kappa k_2 + \rho k_1)}, \quad u_e^2 = \frac{\mu}{(\alpha + (u_e^1)^2)}, \\ U_{0e} &= \frac{\mu\rho k_2}{(\kappa + \kappa k_2 + \rho k_1)}, \end{aligned} \quad (3.4)$$

where  $U_{0e}$  is the steady-state average concentration in the bulk region and  $\mathbf{u}_e \equiv (u_e^1, u_e^2)^T$  is the steady-state intracellular concentration.

We perturb the steady-state solution  $(U_{0e}, u_e^1, u_e^2)$  as

$$U = U_{0e} + e^{\lambda t}\eta, \quad \mathbf{u} = \mathbf{u}_e + e^{\lambda t}\phi, \quad (3.5)$$

where  $\eta \ll 1$  and  $\phi \equiv (\phi_1, \phi_2)^T \ll 1$ . Upon substituting (3.5) into (3.2), we obtain the linearized system

$$\lambda\eta = -\kappa\eta - \rho(k_1\eta - k_2\phi_1), \quad \lambda\phi = J_e\phi + \mathbf{e}_1(k_1\eta - k_2\phi_1), \quad (3.6)$$

where  $J_e$  is the Jacobian matrix of the reaction kinetics  $\mathbf{F}(\mathbf{u}) \equiv (f(u^1, u^2), g(u^1, u^2))^T$  evaluated at the steady-state  $\mathbf{u}_e = (u_e^1, u_e^2)^T$ . Labeling  $(u_e^1, u_e^2) \equiv (v_e, w_e)$  and  $\mathbf{F} = (f(v, w), g(v, w))^T$ , we write (3.6) in matrix form as

$$\mathcal{H}(\lambda)\Psi = \mathbf{0}. \quad (3.7)$$

where  $\Psi \equiv (\eta, \phi_1, \phi_2)^T$  and  $\mathcal{H}(\lambda)$  is the  $3 \times 3$  matrix

$$\mathcal{H}(\lambda) \equiv \begin{pmatrix} -(\kappa + \rho k_1) - \lambda & \rho k_2 & 0 \\ k_1 & (f_v^e - k_2 - \lambda) & f_w^e \\ 0 & g_v^e & (g_w^e - \lambda) \end{pmatrix}. \quad (3.8)$$

Here,  $f_v^e, f_w^e, g_v^e$  and  $g_w^e$  are the partials of  $f$  and  $g$  evaluated at  $\mathbf{u}_e$ . The characteristic polynomial for (3.7) is

$$\lambda^3 + q_1\lambda^2 + q_2\lambda + q_3 = 0, \quad (3.9)$$

with coefficients given by

$$\begin{aligned} q_1 &\equiv (\kappa + k_2 + \rho k_1) - \text{tr}(J_e), \\ q_2 &\equiv \det(J_e) - (\kappa + \rho k_1)\text{tr}(J_e) + k_2(\kappa - g_w^e), \\ q_3 &\equiv (\kappa + \rho k_1)\det(J_e) - \kappa k_2 g_w^e, \end{aligned} \quad (3.10)$$

where  $\det(J_e) = f_v^e g_w^e - f_w^e g_v^e$  and  $\text{tr}(J_e) = f_v^e + g_w^e$  are the determinant and trace of the Jacobian  $J_e$ . For Sel'kov kinetics we readily calculate that  $\det(J_e) = \epsilon_0(\alpha + v_e^2) > 0$  and  $\text{tr}(J_e) = 2w_e v_e - 1 - \epsilon_0(\alpha + v_e^2)$ . By the Routh-Hurwitz criterion for cubic polynomials, we have  $\text{Re}(\lambda) < 0$  if and only if the following three conditions hold:

$$q_1 > 0, \quad q_3 > 0, \quad \text{and} \quad q_1 q_2 > q_3. \quad (3.11)$$

To determine Hopf bifurcation (HB) points, for which  $\lambda_1 = a < 0$ ,  $\lambda_{2,3} = \pm i\omega$ , we must have  $(\lambda - a)(\lambda - i\omega)(\lambda + i\omega) = \lambda^3 - a\lambda^2 + \omega^2\lambda - a\omega^2 = 0$  so that the coefficients in (3.9) must satisfy

$$q_1 > 0, \quad q_3 > 0, \quad \text{and} \quad q_1 q_2 = q_3, \quad (3.12)$$

at the HB points. This criterion is used below to compute HB points with respect to bifurcation parameters.

In the results below, the Sel'kov parameters in (3.3) and the influx and efflux permeabilities are fixed at

$$\alpha = 0.9, \quad \epsilon_0 = 0.15, \quad \mu = 2, \quad \tilde{d}_1 = 0.8, \quad d_2 = 0.2. \quad (3.13)$$

The kinetics parameters  $\alpha$ ,  $\epsilon_0$  and  $\mu$  have been selected so that the local dynamics of each cell is linearly stable when it is isolated from the bulk (i.e.  $\text{tr}(J_e) < 0$ ). Our goal is to seek an oscillatory instability in the intracellular dynamics that is triggered by the global coupling.

Next, we compute HB points of the leading-order ODE system (3.2) using the criteria in (3.12), parameters in (3.13), and with  $D_0 = 0.5$  for  $m = 6$  identical cells. Fixing  $\kappa = 3.2$ , the HB points with respect to the cell density are  $\rho_1 = 0.3548$  and  $\rho_2 = 5.2035$ . Since  $\rho = m/|\Omega|$  and  $m = 6$  is fixed, varying  $\rho$  corresponds to varying the volume  $|\Omega|$  of the domain  $\Omega$ . Similarly, for a fixed cell density  $\rho = 1.4324$  (corresponding to  $m = 6$  cells in the unit sphere), the HB points with respect to the bulk decay parameter  $\kappa$  are  $\kappa_1 = 1.5508$  and  $\kappa_2 = 16.7815$ . These HB points agree with the global bifurcation results shown in Fig. 2, as computed using the numerical bifurcation software MATCONT [29]. On the range of parameters where the steady-state is linearly unstable, we observe from Fig. 2 the existence of a linearly stable periodic solution.

From Fig. 2 we observe that there are no intracellular oscillations when either  $\kappa$  is sufficiently small or large. Since  $\kappa$  is the dimensionless ratio of the decay rate  $k_B$  of the bulk species to the reaction rate  $k_R$  of the local kinetics of the cells (see (1.3)), a small value of  $\kappa$  implies that the rate of intracellular reactions is relatively high

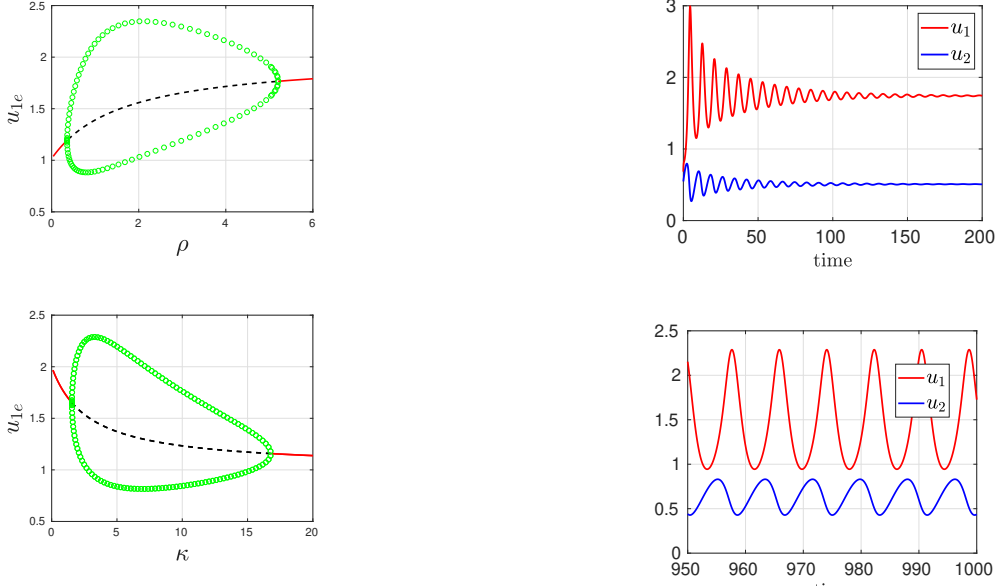


*Figure 2:* Global bifurcation diagrams for the ODE system (3.2) showing steady-states and branches of periodic solutions for  $m = 6$  identical cells, as computed using MATCONT [29], for the Sel'kov kinetics (3.3) with parameters in (3.13) and with  $D_0 = 0.5$ . Top panel: For  $\kappa = 3.2$ , the HB points occur at  $\rho_1 = 0.3548$  and  $\rho_2 = 5.2035$ . Right panel: For the unit sphere where  $\rho = 1.4324$ , the HB points occur at  $\kappa_1 = 1.5508$  and  $\kappa_2 = 16.7814$ . The red-solid and black-dashed lines represent linearly stable and unstable branches, respectively. The green loop represents linearly stable branches of periodic solutions.

231 compared to the decay rate of the bulk species. As a result, the intracellular dynamics tend quickly to the quiescent state since the Sel'kov parameters are chosen so  
232 that the steady-state for each cell is linearly stable when isolated. Alternatively, a large value of  $\kappa$  implies that the  
233 secreted intracellular species has a short length-scale for  
234 decay in the bulk region, making it difficult to have the  
235 strong inter-cellular communication that is needed for  
236 collective oscillations or quorum-sensing behavior.  
237

238 In Fig. 3, we show numerical results computed from  
239 the ODE system (3.2) using *ODE45* in MATLAB [30]  
240 for  $m = 6$  identical cells in the unit sphere where  $\rho =$   
241  $1.4324$ , with parameters in (3.13), and with  $D_0 = 0.5$ .  
242 In the top panel of Fig. 3, where  $\kappa = 1$ , we observe  
243 damped intracellular oscillations leading to a linearly  
244 stable steady-state as predicted by the bifurcation  
245 diagram in the bottom panel of Fig. 2. In contrast, for  
246  $\kappa = 3.2$ , in the middle and bottom panels of Fig. 3 we  
247 observe sustained oscillations that are triggered by the  
248 global coupling. This is consistent with the prediction  
249 in Fig. 2 of a stable periodic solution for  $\kappa = 3.2$ .  
250

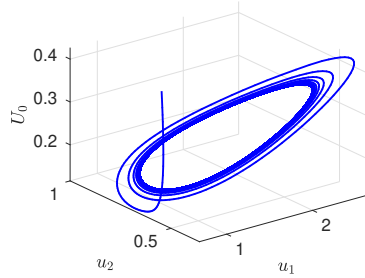


*Figure 3:* Numerical results for the ODE system (3.2) showing the intracellular dynamics for  $m = 6$  identical cells in the unit sphere, where  $\rho = 1.43239$ , for Sel'kov kinetics (3.3), with parameters in (3.13) and with  $D_0 = 0.5$ . Top panel: For  $\kappa = 1$ , damped oscillations occur. Middle panel: For  $\kappa = 3.2$ , there are sustained oscillations. Bottom panel: 3-D plot for  $(U_0, u_1, u_2)$  showing sustained oscillations when  $\kappa = 3.2$ . Result are consistent with the bifurcation diagram in the bottom panel of Fig. 2.

### 3.2. Quorum sensing and phase synchronization

Next, we use the ODE system (3.1) and the Kuramoto order parameter [31] to study quorum sensing and phase synchronization in the intracellular dynamics of a collection of cells as  $\rho$  increases. This order parameter has been used to measure the degree of phase synchrony of coupled non-linear oscillators [31, 22, 21, 24]. Here we use the version given in [22, 21, 24] by

$$R = \left\langle \left| N^{-1} \sum_{j=1}^N \exp[i\theta_j(t)] - \left\langle N^{-1} \sum_{j=1}^N \exp[i\theta_j(t)] \right\rangle \right| \right\rangle, \quad (3.14)$$

253 where  $N$  is the number of oscillators,  $\theta_j(t)$  is the instantaneous phase of the  $j^{\text{th}}$  oscillator, and  $\langle \dots \rangle$  represents average over time. The value of  $R$  ranges from 0 to 1, and measures the level of phase synchronization of the oscillators. When  $R = 1$ , the oscillators are perfectly in phase, and they are perfectly out of phase when  $R = 0$ .

259 To compute  $R$  we first solve the ODEs (3.1) with random initial conditions numerically using *ODE45* in MATLAB [30]. After discarding the solution over the transient period, we fit a single-mode Fourier series expansion to one of the solution components for each cell and compute the instantaneous phase  $\theta_j(t)$  from the coefficients of the series, from which we calculate the phase average  $z = N^{-1} \sum_{j=1}^N e^{i\theta_j}$ . Next, we compute an average of the instantaneous averages  $\langle z \rangle$  over a specified time interval (after the system has reached a quasi steady-state). The modulus of the difference between the instantaneous averages  $z$  and the time-average  $\langle z \rangle$  is computed for each time point, and the corresponding result averaged over time to obtain the order parameter  $R$ , as given in (3.14). In our computations, we set  $R = 0$  when the cells are in a quiescent state or when the amplitude of the oscillations is less than  $1 \times 10^{-4}$ .

276 In our examples below, the cell population  $m = 1000$  277 is fixed and will be taken to be a mixture of identical 278 and *defective* cells, where the heterogeneous cells have 279 a different Sel'kov kinetic parameter  $\alpha$  in (3.3). Since 280  $\rho \equiv m/|\Omega|$  and  $m$  is fixed, a change in  $\rho$  represents a 281 change in the domain volume  $|\Omega|$ . In Fig. 4 we plot the 282 order parameter  $R$  and the amplitude of oscillation for 283 1000 identical cells versus  $\rho$ . We observe that there are 284 no oscillations when  $\rho$  is small and that there is a sudden 285 switch-like transition to perfect phase synchronization 286 when  $\rho \approx 0.36$ . This phase synchrony is maintained 287 until  $\rho \approx 5.28$  where there is a further switch-like 288 transition that leads to oscillator death and a quiescent state.

289 To qualitatively interpret this behavior, there are no synchronous intracellular oscillations when  $\rho$  is small since 290 the domain is too large for them to communicate effectively 291 through the diffusing bulk signal. As  $\rho$  increases, 292 the domain volume shrinks, thereby bringing the cells 293 closer together and ultimately leading to synchronous 294 oscillations and quorum-sensing behavior. However, as 295  $\rho$  continues to increase, the synchronous oscillations 296 are quenched because the cells become more tightly 297 packed, with a smaller bulk region, and so effectively 298 behave like a single giant cell. Since the Sel'kov 299 parameters (3.13) are chosen so that the steady-state of an 300 individual cell is linearly stable when isolated from the 301 bulk, the steady-state for the giant cell is also linearly 302

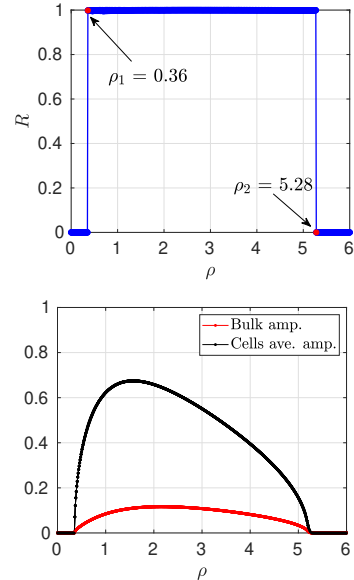


Figure 4: The degree of phase synchronization and amplitude of oscillation for 1000 identical cells, computed from the ODEs (3.1) with Sel'kov kinetics (3.3), parameters in (3.13), and with  $D_0 = 0.5$  and  $\kappa = 3.2$ . Top panel: The Kuramoto order parameter  $R$  in (3.14) versus the cell density parameter  $\rho$ . Synchronous oscillations are triggered at  $\rho_1 = 0.36$  and extinguished at  $\rho_2 = 5.28$ . Bottom panel: The average amplitude of oscillation in the cells (black) and in the bulk region (red) versus  $\rho$ .

303 stable.

304 In Fig. 5, we present similar results for 500 identical 305 and 500 *defective* cells. The identical cells have param- 306 eters in (3.13), while for the defective cells the Sel'kov 307 kinetic parameter  $\alpha$  is selected uniformly from the 308 interval  $0.92 < \alpha < 0.95$ . From Fig. 5, we observe 309 that synchronous oscillations are triggered at  $\rho = 0.44$  310 and quenched at  $\rho = 4.49$ , which provides (as expected) 311 a smaller range of  $\rho$  where phase synchrony occurs as 312 compared to the case of 1000 identical cells. For 200 313 identical and 800 defective cells, in Fig. 6 we show that 314 the range in  $\rho$  where perfect phase synchrony occurs is 315 further decreased as compared to that in Fig. 5.

316 In summary, we conclude from Figs. 4–6 that the cell 317 population density plays a dual role of both triggering 318 and quenching synchronous intracellular oscillations. 319 When it triggers oscillations, it does so through quo- 320 rum sensing. This is similar to the result obtained in 321 Section 4.2 of [24]. Moreover, as the percentage of 322 defective cells in the population increases, the range of 323  $\rho$  for which synchronous oscillations are predicted de- 324 creases, as does the amplitude of intracellular and bulk 325 oscillations. Overall, this indicates, as expected, that 326 effective communication leading to synchronous intra-

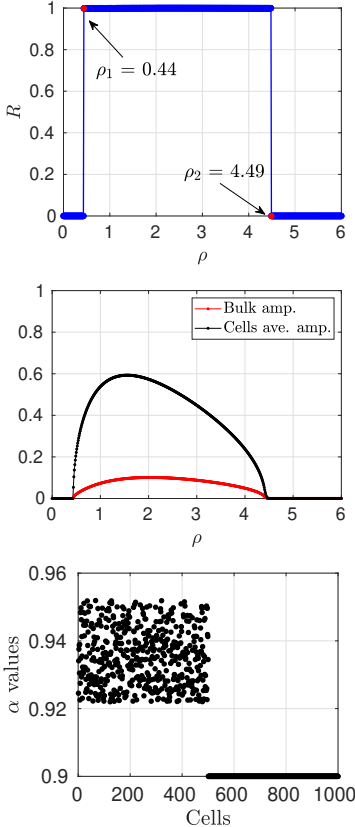


Figure 5: The degree of phase synchronization and amplitude of oscillation for 500 identical and 500 defective cells, computed from the ODEs (3.1) for Sel'kov kinetics (3.3) with  $D_0 = 0.5$  and  $\kappa = 3.2$ . The identical cells have parameters in (3.13). The kinetic parameter  $\alpha$  for the defective cells are selected uniformly from the interval  $0.92 < \alpha < 0.95$ , with  $\alpha = 0.9$  for the identical cells. Top panel: The Kuramoto order parameter (3.14) with respect to  $\rho$ . Phase synchronization is triggered at  $\rho_1 = 0.44$  and extinguished at  $\rho_2 = 4.49$ . Middle panel: The average amplitude of oscillation in the cells (black) and in the bulk region (red) with respect to  $\rho$ . Bottom panel: Values of  $\alpha$  for the 1000 cells.

327 cellular oscillations is more difficult to achieve among a  
328 population of non-identical cells.

#### 329 4. Effect of location on intracellular dynamics

330 Within the unit sphere, we now examine the effect on  
331 the intracellular dynamics of including the  $O(\varepsilon)$  correc-  
332 tion terms in the ODEs (2.18) that incorporates the spa-  
333 tial configuration of the cells. In order to clearly illus-  
334 trate quorum-sensing and diffusion-mediated communi-  
335 cation through the aid of global bifurcation diagrams we  
336 will focus our case study below to a small population of  
337  $m = 6$  cells.

The effect of cell location is encoded by the Neumann

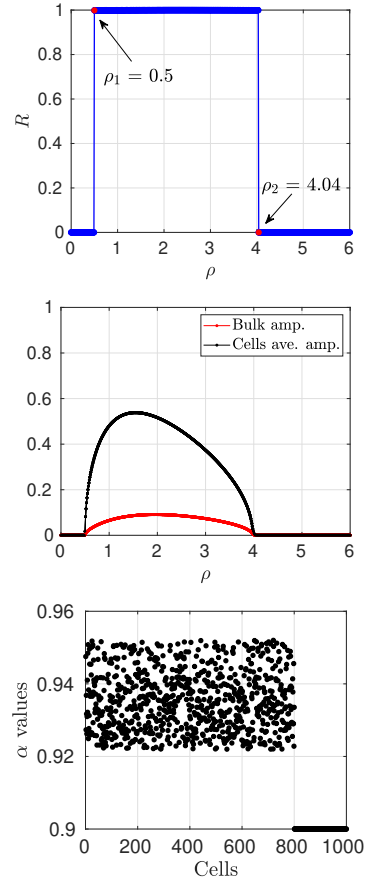


Figure 6: Same caption as in Fig. 5 except that there are now 200 identical and 800 defective coupled cells. Synchronous oscillations are now triggered at  $\rho_1 = 0.5$  and extinguished at  $\rho_2 = 4.04$ .

Green's function satisfying (2.10), which is given for the unit sphere by (cf. [32])

$$G(\mathbf{x}; \mathbf{x}_j) = \frac{1}{4\pi|\mathbf{x} - \mathbf{x}_j|} + \frac{1}{4\pi|\mathbf{x}||\mathbf{x}' - \mathbf{x}_j|} + \frac{(|\mathbf{x}|^2 + |\mathbf{x}_j|^2)}{6|\Omega|} + \frac{1}{4\pi} \log\left(\frac{2}{1 - \mathbf{x} \cdot \mathbf{x}_j + |\mathbf{x}||\mathbf{x}' - \mathbf{x}_j|}\right) - \frac{7}{10\pi}, \quad (4.1a)$$

where the regular part of  $G$  is given by

$$R_j \equiv R(\mathbf{x}_j) = \frac{1}{4\pi(1 - |\mathbf{x}_j|^2)} + \frac{1}{4\pi} \log\left(\frac{1}{1 - |\mathbf{x}_j|^2}\right) + \frac{|\mathbf{x}_j|^2}{4\pi} - \frac{7}{10\pi}, \quad (4.1b)$$

In (4.1),  $|\Omega| = 4\pi/3$  and  $\mathbf{x}' = \mathbf{x}/|\mathbf{x}|^2$  is the image point to  $\mathbf{x}$  outside the sphere. With this explicit result, the Neu-

mann Green's matrix  $\mathcal{G}$  in (2.13) can be readily evaluated. Below we will consider three specific cell configurations within the unit sphere: symmetrically located cells on the surface of a concentric sphere, arbitrarily located cells on the surface of a concentric sphere, and arbitrarily located cells within the unit sphere.

#### 4.1. Symmetrically located cells on a concentric sphere

We consider  $m = 6$  identical cells of a common radius  $\varepsilon$ , symmetrically located on the surface of a concentric sphere of radius  $r_0$  with  $0 < r_0 < 1$ , such as illustrated in Fig. 7 when  $r_0 = 0.5$ .

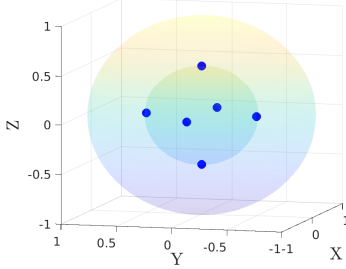


Figure 7: A configuration of six symmetrically located cells (in blue) on the surface of a concentric sphere of radius  $r_0 = 0.5$  within the unit sphere. The cell locations are:  $(r_0, 0, 0)$ ,  $(-r_0, 0, 0)$ ,  $(0, r_0, 0)$ ,  $(0, -r_0, 0)$ ,  $(0, 0, r_0)$  and  $(0, 0, -r_0)$ .

For this cell configuration, the Neumann Green's matrix  $\mathcal{G}$  is symmetric and cyclic, so that it has the eigenpair

$$\mathcal{G}\mathbf{e} = \sigma\mathbf{e}; \quad \mathbf{e} \equiv (1, \dots, 1)^T, \quad \sigma = R_1 + \sum_{j=2}^m G(\mathbf{x}_1; \mathbf{x}_j). \quad (4.2)$$

Here,  $\sigma \equiv \sigma(r_0)$ , where  $r_0$  is the distance from the origin to the radius of the sphere on which the cells are located.

As a result, for identical cells with this configuration we seek a solution to (2.18) where  $\mathbf{u}_j = \mathbf{u} = (u^1, u^2)^T$  for  $j = 1, \dots, m$ . Upon using  $\mathbf{e}^T \mathcal{G} \mathbf{e} = m\sigma$ , we readily derive that (2.18) reduces to

$$U'_0 = -\kappa U_0 - \rho(k_1 U_0 - k_2 u^1) - 4\pi\varepsilon\rho\tilde{c}k_1\sigma, \quad (4.3)$$

$$\frac{d\mathbf{u}}{dt} = \mathbf{F}(\mathbf{u}) + \mathbf{e}_1(k_1 U_0 - k_2 u^1) + 4\pi\varepsilon\tilde{c}k_1\sigma\mathbf{e}_1,$$

where  $\mathbf{e}_1 \equiv (1, 0)^T$ . Here  $\rho = m/|\Omega|$  is the cell density parameter while  $k_1$ ,  $k_2$ , and  $\tilde{c}$  are given by

$$k_1 \equiv \frac{4\pi D_0 \tilde{d}_1}{\tilde{d}_1 + D_0}, \quad k_2 \equiv \frac{4\pi D_0 d_2}{\tilde{d}_1 + D_0}, \quad (4.4)$$

$$\tilde{c} \equiv \frac{1}{4\pi D_0}(k_2 u^1 - k_1 U_0).$$

By substituting  $\tilde{c}$  from (4.4) into (4.3), we obtain a three-component ODE system for  $(U_0, u^1, u^2)$  given by

$$U'_0 = -(\kappa + \rho\chi) U_0 + \rho\xi u^1, \quad (4.5)$$

$$\frac{d\mathbf{u}}{dt} = \mathbf{F}(\mathbf{u}) + (\chi U_0 - \xi u^1)\mathbf{e}_1,$$

where the newly introduced parameters  $\chi \equiv \chi(r_0)$  and  $\xi \equiv \xi(r_0)$  are defined in terms of  $\varepsilon\sigma(r_0)/D$  by

$$\chi \equiv k_1 - \frac{\varepsilon\sigma}{D_0}k_1^2, \quad \xi \equiv k_2 - \frac{\varepsilon\sigma}{D_0}k_1 k_2. \quad (4.6)$$

The ODEs (4.5) have a similar structure to the ODE system in (3.2). As such we now perform a HB analysis on (4.5) following the approach used in §3.1. With Sel'kov kinetics (3.3), the steady-state of (4.5) is

$$u_e^1 = \frac{\mu(\kappa + \chi\rho)}{(\kappa(1 + \xi) + \rho\chi)}, \quad u_e^2 = \frac{\mu}{(\alpha + (u_e^1)^2)}, \quad (4.7)$$

$$U_{0e} = \frac{\mu\rho\xi}{(\kappa(1 + \xi) + \rho\chi)}.$$

Next, we introduce a perturbation of the steady-state as

$$U = U_{0e} + e^{\lambda t}\eta, \quad \mathbf{u} = \mathbf{u}_e + e^{\lambda t}\phi, \quad (4.8)$$

where  $\eta \ll 1$  and  $\phi \equiv (\phi_1, \phi_2)^T \ll 1$ . Upon substituting (4.8) into (4.5), we write the linearized system in matrix form as

$$\mathcal{M}(\lambda)\Psi = \mathbf{0}, \quad (4.9)$$

where  $\Psi \equiv (\eta, \phi_1, \phi_2)^T$  and  $\mathcal{M}(\lambda)$  is the  $3 \times 3$  matrix

$$\mathcal{M}(\lambda) \equiv \begin{pmatrix} -(\kappa + \rho\chi) - \lambda & \rho\xi & 0 \\ \chi & (f_v^e - \xi - \lambda) & f_w^e \\ 0 & g_v^e & (g_w^e - \lambda) \end{pmatrix}. \quad (4.10)$$

Here,  $(v, w)^T \equiv (u^1, u^2)^T$ ,  $f_v^e$ ,  $f_w^e$ ,  $g_v^e$  and  $g_w^e$  are the partials of  $f(v, w)$  or  $g(v, w)$  evaluated at the steady-state  $\mathbf{u}_e = (v_e, w_e)^T$ . The characteristic polynomial for  $\lambda$  is

$$\lambda^3 + \gamma_1\lambda^2 + \gamma_2\lambda + \gamma_3 = 0, \quad (4.11)$$

with coefficients given by

$$\gamma_1 = (\kappa + \xi + \rho\chi) - \text{tr}(J_e),$$

$$\gamma_2 = \det(J_e) - (\kappa + \rho\chi)\text{tr}(J_e) + \xi(\kappa - g_w^e), \quad (4.12)$$

$$\gamma_3 = (\kappa + \rho\chi)\det(J_e) - \kappa\xi g_w^e,$$

where  $\det(J_e) = \epsilon_0(\alpha + v_e^2) > 0$  and  $\text{tr}(J_e) = 2w_e v_e - 1 - \epsilon_0(\alpha + v_e^2)$  are the determinant and trace of the Jacobian matrix  $J_e$  of the Sel'kov kinetics evaluated at the steady-state  $\mathbf{u}_e$ . Similar to the analysis in §3.1, we conclude by the Routh-Hurwitz criterion that a HB point for the linearization must satisfy

$$\gamma_1 > 0, \quad \gamma_3 > 0, \quad \text{and} \quad \gamma_1 \gamma_2 = \gamma_3. \quad (4.13)$$

This HB criterion is used below to determine how the triggering of oscillatory instabilities depends on  $D_0$  and  $r_0$ . Global branches of steady-state and periodic solutions for (4.5) are computed using MATCONT [29].

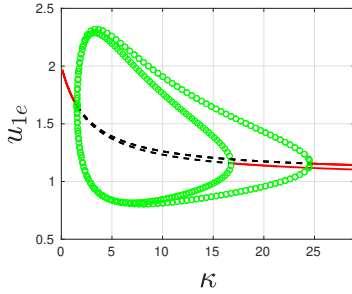


Figure 8: Global bifurcation diagrams for the ODE system (4.5) versus the bulk decay rate  $\kappa$  showing branches of steady-states and periodic solutions computed using MATCONT [29] for  $m = 6$  identical cells, with parameters in (3.13) and with  $\rho = 1.43239$  and  $D_0 = 0.5$ . The outer loop is for cells of radius  $\varepsilon = 0.05$ , symmetrically-spaced on a concentric sphere of radius  $r_0 = 0.25$  within the unit sphere, with locations given in the caption of Fig. 7. The HB bifurcation points are  $\kappa_1 = 1.5518$  and  $\kappa_2 = 24.5774$ . The inner loop is for the leading-order dynamics (3.2) when  $\varepsilon = 0$  (same as bottom panel of Fig. 2), where HB bifurcations occur at  $\kappa_1 = 1.551$  and  $\kappa_2 = 16.7814$ . The red-solid and black-dashed lines represent linearly stable and unstable steady-state branches, respectively. The green loops represent linearly stable branches of periodic solutions.

In Fig. 8 we plot a global bifurcation diagram for the ODE system (4.5) versus the bulk decay rate  $\kappa$  for  $D_0 = 0.5$ ,  $\rho = 1.4324$ , and for  $m = 6$  symmetrically-spaced identical cells on a ring of radius  $r_0 = 0.25$  with a cell radius  $\varepsilon = 0.05$ . The Sel'kov parameters and permeabilities are as in (3.13). In this figure, we have overlayed the corresponding bifurcation diagram shown in the bottom panel of Fig. 2 that was based on the leading-order dynamics (3.2) when  $\varepsilon = 0$ . From Fig. 8 we observe that there are values of  $\kappa$  for which linearly stable periodic solutions exist for the symmetric cells but not for the leading-order dynamics. The existence of this significantly larger upper range of  $\kappa$  where periodic solutions can occur is attributed to the fact that  $r_0 = 0.25$  is rather small, and so the cells are still able to readily communicate through the bulk diffusion field

even when there is a stronger decay of the bulk signal. Overall, Fig. 8 shows clearly that the inclusion of the  $O(\varepsilon)$  terms in the ODEs (4.5), incorporating the effect of weak spatial heterogeneity, can be a significant factor in determining whether or not intracellular oscillations can occur.

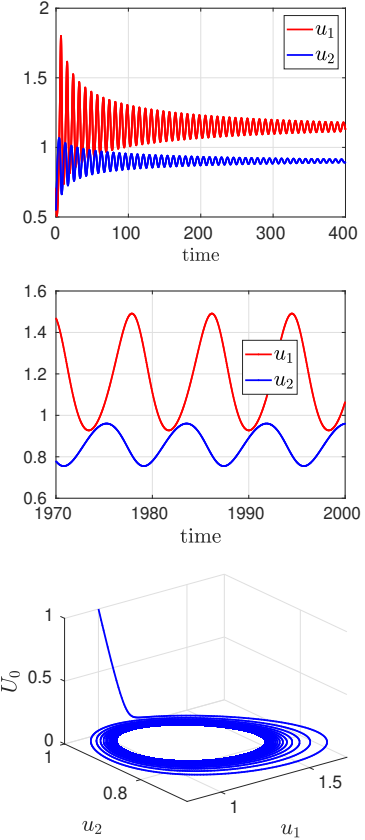


Figure 9: Numerical simulation of ODE dynamics using ODE45 in MATLAB for the parameters in the caption of Fig. 8 with  $\kappa = 18.5$ . Top panel: For the leading-order dynamics (3.2) there is a slow decay to the linearly stable steady-state. Middle panel: For (4.5) with symmetrically-spaced cells with ring radius  $r_0 = 0.25$  and cell radius  $\varepsilon = 0.05$ , there are sustained intracellular oscillations. Bottom panel: 3-D plot showing the sustained oscillatory dynamics in the middle panel with respect to the three variables.

In Fig. 9 we confirm the predictions of the global bifurcation diagram in Fig. 8. For  $\kappa = 18.5$ , the intracellular dynamics are predicted to have a linearly stable steady-state for the leading-order dynamics (3.2). In contrast, for this same value of  $\kappa$ , synchronous intracellular oscillations are predicted for (4.5) when the  $O(\varepsilon)$  spatial effects are included. These two predictions are confirmed from the ODE dynamics shown in the top and middle panels of Fig. 9. In the bottom panel of Fig. 9 we show a 3-D plot of the sustained oscillation for (4.5), which shows that the amplitude of bulk oscillations is rather

390 small as compared to those in the cells.

391 In the top panel of Fig. 10 we study the effect on the  
 392 global bifurcation diagrams for (4.5) of varying the ring  
 393 radius  $r_0$  for  $m = 6$  symmetrically-spaced cells. The  
 394 remaining parameters are as in the caption of Fig. 8.  
 395 From this figure, we observe that the smallest range of  
 396 the bulk decay parameter  $\kappa$  for which intracellular os-  
 397 cillations are predicted is for  $r_0 = 0.5$ , followed by  
 398  $r_0 = 0.85$ , and then  $r_0 = 0.25$ . When  $r_0 = 0.5$ , the cells  
 399 are far from each other and from the domain boundary,  
 400 so that it is more difficult to trigger synchronous oscil-  
 401 lations through the bulk medium than for  $r_0 = 0.25$ . For  
 402  $r_0 = 0.85$ , although the cells are far from each other,  
 403 each cell is relatively close to an “image” cell through  
 404 the reflecting boundary of the domain, resulting in a  
 405 pairwise intracellular communication. In the bottom  
 406 panel of Fig. 10, we plot the two HB points in  $\kappa$  ver-  
 407 sus  $r_0$ , as computed using two-parameter continuation  
 408 in MATCONT [29] (solid black curves) and from the  
 409 HB criteria in (4.13) (blue dots). In this figure, linearly  
 410 stable periodic solutions exist in the region between the  
 411 two black curves. For  $\varepsilon = 0.05$ , we observe that the  
 412 smaller HB value of  $\kappa$  is rather insensitive to  $r_0$  provided  
 413 that  $2\varepsilon = 0.1 < r_0 < 1 - 2\varepsilon = 0.9$ . Since the asymptotic  
 414 theory leading to the ODEs (4.5) is valid only for  
 415 well-separated cells, we require  $O(\varepsilon) \ll r_0 \ll 1 - O(\varepsilon)$ .  
 416 From the bottom panel of Fig. 10, the smallest range of  
 417  $\kappa$  where periodic solutions occur is when  $r_0 = 0.6$ , with  
 418 HB points at  $\kappa_1 \approx 1.55$  and  $\kappa_2 \approx 13.7$ .

419 Fig. 11 shows the time-dynamics of the ODEs (4.5) for  
 420 three pairs of  $(r_0, \kappa)$  and with remaining parameter val-  
 421 ues as in the caption of Fig. 10. The dynamics shown  
 422 agree with the results predicted from the global bifurca-  
 423 tion diagrams in Fig. 10.

424 Next, we investigate the effect of the bulk diffusivity  
 425  $D_0$  on the dynamics. In the top panel Fig. 12 we plot  
 426 the global bifurcation diagram for (4.5) versus  $D_0$  for  
 427 two values of  $\varepsilon$  when  $r_0 = 0.25$  and  $\kappa = 18.5$ . When  
 428 accounting for a finite cell radius, we observe that the  
 429 range of  $D_0$  where oscillations are predicted is larger  
 430 than for the leading-order ODE system (3.2) where  
 431  $\varepsilon = 0$ . In the bottom panel of Fig. 12 we plot the two  
 432 HB points in  $D_0$  for each  $r_0$  in  $0 < r_0 < 1$  as computed  
 433 from MATCONT from (4.5) or from our HB criteria  
 434 (4.13). Linearly stable periodic solutions exist in the  
 435 region bounded by the black curves. Since our asymptotic  
 436 theory is valid only when  $O(\varepsilon) \ll r_0 \ll 1 - O(\varepsilon)$ , we ne-  
 437 glect the horizontal line near  $r_0 = 1$  in the bottom panel  
 438 of Fig. 12. From this figure, we observe that in the com-  
 439 pletely well-mixed limit, for which  $D_0 \rightarrow \infty$ , no intra-

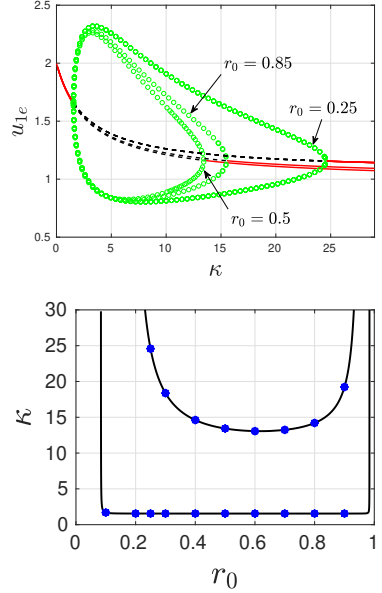


Figure 10: Top panel: Global bifurcation diagrams for the ODE system (4.5) versus  $\kappa$  for three values of ring radii  $r_0$ , as computed using MATCONT [29] for  $m = 6$  symmetrically-spaced identical cells of radii  $\varepsilon = 0.05$ , with parameters in (3.13) and with  $\rho = 1.43239$  and  $D_0 = 0.5$ . The HB points are:  $\kappa_1 = 1.5518$ ,  $\kappa_2 = 24.577375$  for  $r_0 = 0.25$ ;  $\kappa_1 = 1.5504$ ,  $\kappa_2 = 13.5721$  for  $r_0 = 0.5$ ;  $\kappa_1 = 1.5506$ ,  $\kappa_2 = 15.5074$  for  $r_0 = 0.85$ . Bottom panel: Two-parameter HB continuation for  $\kappa$  versus  $r_0$ . The black curves are the HB boundaries computed from MATCONT. The blue dots are based on the HB criteria in (4.13). Linearly stable periodic solutions exist in the region between the two black curves. The asymptotic theory is valid only when  $O(\varepsilon) \ll r_0 \ll 1 - O(\varepsilon)$ , and so the vertical lines are not relevant.

cellular oscillations will occur when  $0.2 < r_0 < 0.8$ , as the bulk signal is washed out. However, for a finite  $D_0$  in some range, intracellular oscillations do occur. We suggest that this can be interpreted as *diffusion-sensing* behavior. For  $r_0 = 0.25$  and  $\kappa = 18.5$ , the time-dynamics computed from (4.5) shown in Fig. 13 confirm the predictions of our bifurcation diagram in the top panel of Fig. 12 for three pairs of  $(\varepsilon, D_0)$ .

#### 4.2. Arbitrarily located cells on a concentric sphere

We now consider  $m = 6$  identical, but non-equally spaced cells on a concentric ring of radius  $r_0$  within the unit disk. For identical cells, for which  $k_{1j} = k_1$  and  $k_{2j} = k_2$  for  $j = 1, \dots, m$ , the ODE system (2.18) reduces to

$$U'_0 = -\kappa U_0 + \frac{\rho}{m} \sum_{j=1}^m (k_2 u_j^1 - k_1 U_0) \quad (4.14a)$$

$$- \frac{4\pi\rho k_1 \varepsilon}{m} \sum_{j=1}^m (\mathcal{G}\mathbf{c})_j, \quad (4.14b)$$

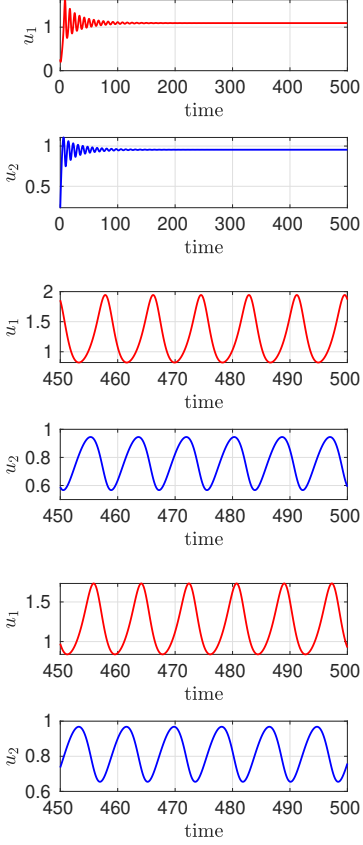


Figure 11: Numerical simulations of ODE dynamics for (4.5) for the parameters in the caption of Fig. 10. Top panels:  $r_0 = 0.5$  and  $\kappa = 23$  (decaying oscillations). Middle panels:  $r_0 = 0.5$  and  $\kappa = 7.5$  (sustained oscillations). Bottom panel:  $r_0 = 0.25$  and  $\kappa = 20$  (sustained oscillations). The results agree with our predictions in the bifurcation diagrams of Fig. 10.

which is coupled to the intracellular dynamics by

$$\frac{d\mathbf{u}_j}{dt} = \mathbf{F}_j(\mathbf{u}_j) - \mathbf{e}_1(k_2 u_j^1 - k_1 U_0) + 4\pi k_1 \varepsilon \mathbf{e}_1(\mathcal{G}\bar{\mathbf{c}})_j, \quad (4.14c)$$

for  $j = 1, \dots, m$ , where  $\mathbf{e}_1 = (1, 0)^T$ ,  $\rho = m/|\Omega|$  is the cell density parameter,  $\varepsilon$  is the common radius of the cells, and  $\mathcal{G}$  is the Neumann Green's matrix of (2.13), which depends the spatial configuration of the cells. In (4.14),  $k_1$  and  $k_2$  are defined in (4.4), and  $\bar{\mathbf{c}}$  is given by

$$\bar{c}_j = \frac{1}{4\pi D_0}(k_2 u_j^1 - k_1 U_0), \quad \bar{\mathbf{c}} \equiv (\bar{c}_1, \dots, \bar{c}_m)^T. \quad (4.14d)$$

For  $m = 6$ , (4.14) is an ODE system of dimension 13. For all the results and figures in the subsection, we use Sel'kov kinetics (3.3) with parameters and permeabilities as in (3.13). The cell centers are given in Table 1

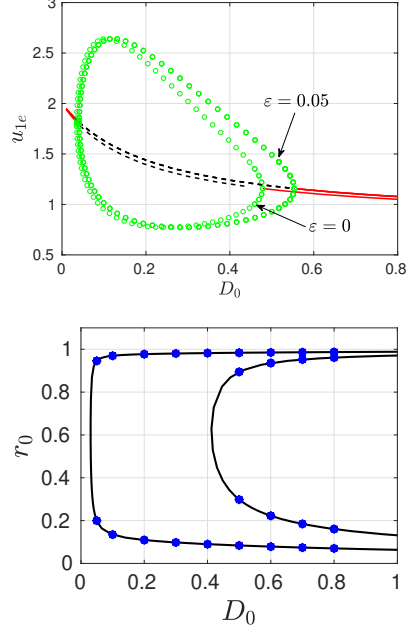


Figure 12: Top panel: Global bifurcation diagrams when  $\kappa = 18.5$  and  $r_0 = 0.25$  for the ODE system (4.5) versus  $D_0$  for  $\varepsilon = 0.05$  and for the leading-order dynamics (3.2) where  $\varepsilon = 0$ , as computed using MATCONT [29]. The remaining parameters are in (3.13) with  $\rho = 1.43239$ . The range in  $D_0$  where oscillations occur is larger when  $\varepsilon = 0.05$ . Bottom panel: Two-parameter HB continuation for  $D_0$  versus  $r_0$  when  $\varepsilon = 0.05$ . The black curves are the HB boundaries computed with MATCONT, while the blue dots were obtained using the HB criteria in (4.13). Linearly stable periodic solutions exist in the region enclosed by the black curves. The horizontal line near  $r_0 = 1$  is not relevant as it signifies the breakdown of the well-separated cell assumption that is required for the derivation of the ODE system.

of Appendix B.1. A schematic illustration of the cell configurations for  $r_0 = 0.5$  and  $r_0 = 0.85$  is shown in Fig. 14. Our goal is to determine the effect on intracellular oscillations of the new arrangement of cells.

In Fig. 15 we compare the global bifurcation diagrams versus  $\kappa$  for the leading-order dynamics, computed using (3.2), with those for either symmetrically- or arbitrarily-spaced cells on a concentric sphere of radius  $r_0 = 0.25$  and cell radius  $\varepsilon = 0.05$ , as computed from either (4.5) or (4.14), respectively. For these three scenarios, we observe that the largest range of  $\kappa$  for which linearly stable periodic solutions exist is for arbitrarily-located cells. This increased range is likely due to the fact that for arbitrarily-spaced cells, there is a pair of cells on the surface of the concentric sphere that are closer than when the cells have maximum inter-cell distance, such as is the case for the symmetrically-spaced configuration. Cells that are in closer proximity can trigger intracellular oscillations even when the bulk

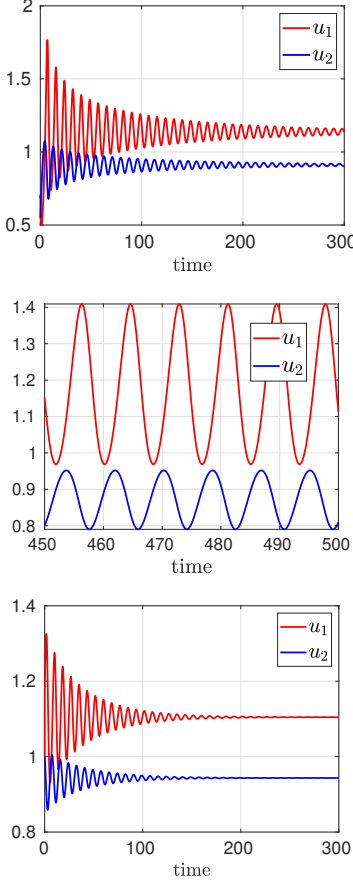


Figure 13: Numerical simulations of ODE dynamics for (4.5) for the parameters in the caption of Fig. 12 with  $r_0 = 0.25$  and  $\kappa = 18.5$ . Top panel:  $\varepsilon = 0$  and  $D_0 = 0.52$  (decaying oscillations). Middle panel:  $\varepsilon = 0.05$  and  $D_0 = 0.52$  (sustained oscillations). Bottom panel:  $\varepsilon = 0.05$  and  $D_0 = 0.7$  (sustained oscillations). The results agree with our predictions in the bifurcation diagrams of Fig. 12.

decay rate  $\kappa$  increases.

In Fig. 16, we show the time-dynamics for the ODE systems (4.5) and (4.14) for a few values of  $\kappa$  that confirm predictions from the bifurcation diagrams of Fig. 15. In this figure, the colors of the curves correspond to the color codes for the cells in Fig. 14 and Table 1. In the top two panels, where  $\kappa = 28$ , we observe a slow synchronous oscillatory decay to the linearly stable steady-state for the symmetrically-spaced cell configuration. However, when  $\kappa = 28$ , from the middle two panels in Fig. 16 we observe roughly synchronous intracellular oscillations for the arbitrarily-spaced pattern. Finally, in the bottom two panels, for  $\kappa = 36$  and arbitrarily-spaced cells, we observe a slow decay of intracellular oscillations to the linearly stable steady-state.

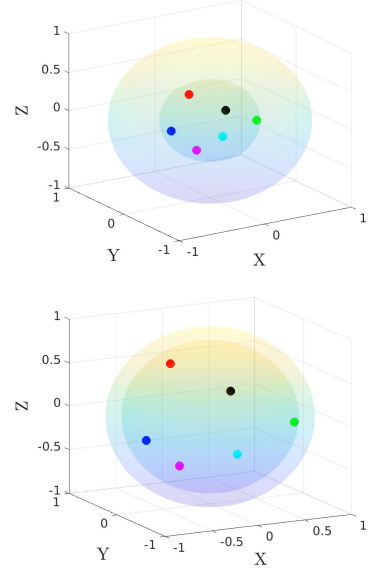


Figure 14: Schematic plot for  $m = 6$  identical, but non-equally spaced, cells centered on a concentric sphere of radius  $r_0 = 0.5$  (top panel) and  $r_0 = 0.85$  (bottom panel) within the unit sphere. The cell centers can be generated from Table 1 of Appendix B.1 for a given  $r_0$ . The color codes are for easy referencing.

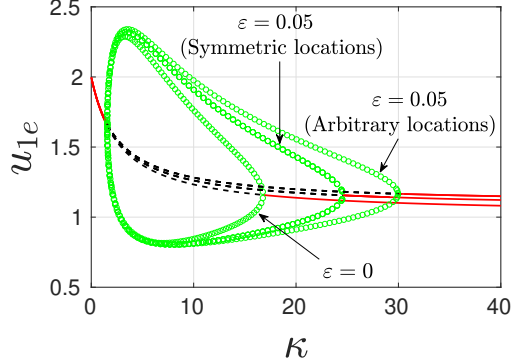


Figure 15: Global bifurcation diagrams versus  $\kappa$  comparing the range where intracellular oscillations occur for either the leading-order dynamics, symmetrically-spaced cells, or arbitrarily-spaced cells, as computed from (3.2), (4.5) and (4.14), respectively, using MATCONT [29]. Parameters as in (3.13) with  $\rho = 1.4324$  and  $D_0 = 0.5$ . The concentric ring has radius  $r_0 = 0.25$  and  $\varepsilon = 0.05$ . The green loops representing periodic solutions for the leading-order dynamics and for symmetrically-spaced cells are as in Fig. 8. For arbitrarily-spaced cells, with cell locations generated from Table 1, the HB points are at  $\kappa_1 = 1.5525$  and  $\kappa_2 = 29.9604$ .

Next, for arbitrarily-spaced cells, we study the effect of the radius  $r_0$  of the concentric sphere on which the cells are located. The global bifurcation diagrams are shown in the top panel of Fig. 17, while in the bottom panel

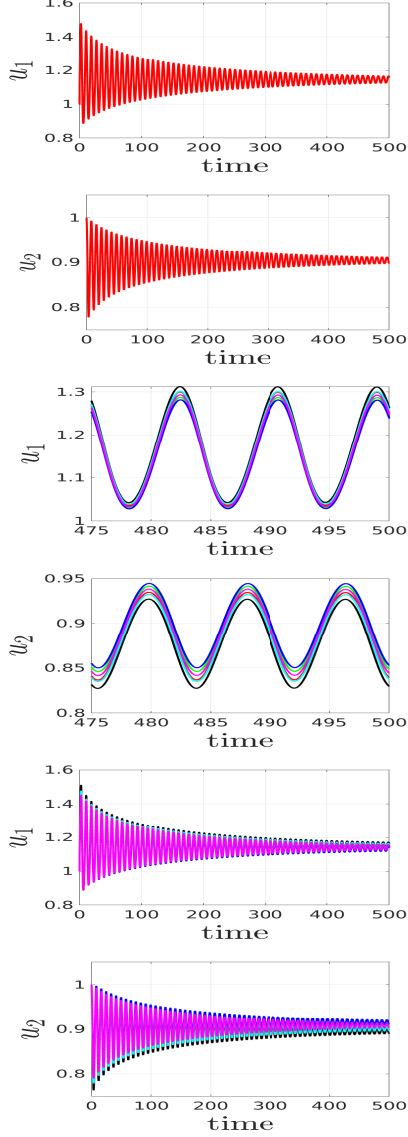


Figure 16: Numerical simulations of ODE dynamics for (4.5) and (4.14) computed using MATLAB for the parameters in the caption of Fig. 15. Top two rows: symmetrically-spaced cells with  $\kappa = 28$ , showing decaying oscillations. Middle two rows: arbitrarily-spaced cells with  $\kappa = 28$ , showing sustained and nearly synchronous oscillations. Bottom two rows: The oscillations for arbitrarily-spaced cells now undergo a slow decay to the steady-state when  $\kappa = 36$ . Colors correspond to the color codes for the cells in Fig. 14 and Table 1.

of Fig. 17 we plot the HB bifurcation points  $\kappa$  versus  $r_0$  using two-parameter continuation. These bifurcation diagrams have a very similar qualitative dependence on  $r_0$  as for the bifurcation plots shown in Fig. 10 for the case where the cells are symmetrically-spaced.

In the global bifurcation diagrams of Fig. 18, we il-

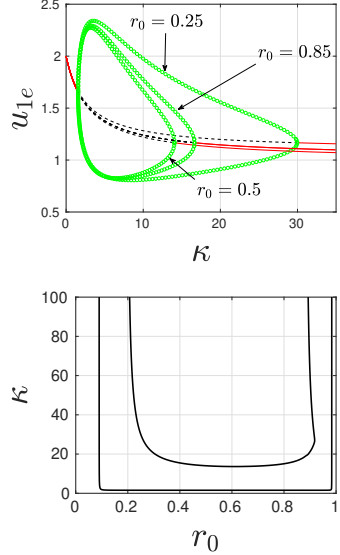


Figure 17: Top panel: Global bifurcation diagrams for the ODE system (4.14) versus  $\kappa$  for three values of ring radii  $r_0$ , as computed using MATCONT [29] for  $m = 6$  arbitrarily-spaced identical cells on a ring, with locations as generated from Table 1, with  $\rho = 1.4329$  and  $D_0 = 0.5$ . For these values of  $r_0$ , the largest range of  $\kappa$  where intracellular oscillations occur is for  $r_0 = 0.25$ . Bottom panel: Two-parameter HB continuation for  $\kappa$  versus  $r_0$  computed from MATCONT. Linearly stable periodic solutions exist in the region between the two black curves. The vertical lines are not relevant as they signify the breakdown of the well-separated cell assumption.

lustrate a qualitatively new behavior that occurs for  $r_0 = 0.85$  when we further extend the range of  $\kappa$ . In particular, we observe that there is an additional HB point at  $\kappa_3 = 35.0067$ . As shown in Fig. 18, linearly stable periodic solutions are predicted when  $1.5509 \leq \kappa \leq 16.6489$  and for  $\kappa \geq 35.0067$ . We emphasize that periodic solutions do not exist for such large values of  $\kappa$  when either  $r_0 = 0.25$  and  $r_0 = 0.5$ .

In Fig. 19 we show results from numerical simulations of the ODE system (4.14) that support the predictions from the global bifurcation diagram in Fig. 18. In particular, in the top two rows where  $\kappa = 5$ , synchronous oscillations are observed in the entire cell population. In the middle two rows where  $\kappa = 25$ , damped oscillations occur. However, in the bottom two rows where  $\kappa = 45$ , we observe that asynchronous intracellular oscillations occur. In particular, the green, cyan, and blue cells synchronize their dynamics, while the red, black and magenta cells also synchronize. However, the dynamics of these two groups of cells are out of phase. We believe that the grouping and synchronization of the cells is based on their spatial proximity, although it is unclear why there are only two sub-groups. From Table 2, we ob-

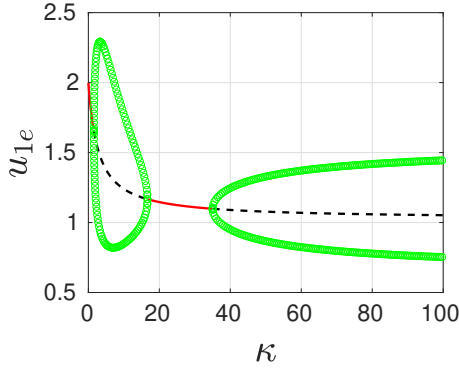


Figure 18: Global bifurcation diagrams for the ODE system (4.14) versus  $\kappa$ , as computed using MATCONT [29] for  $m = 6$  arbitrarily-spaced identical cells located on a ring of radius  $r_0 = 0.85$ , with cell locations generated from Table 1. The remaining parameters are the same as in Fig. 17. There are now three HB bifurcation points at  $\kappa_1 = 1.5509$ ,  $\kappa_2 = 16.6489$  and  $\kappa_3 = 35.0067$

serve that the red, black, and magenta cells are closest to each other, while the green, cyan, and blue are also closest to each other. As  $\kappa$  is increased, the cell-cell distances become an increasingly important factor in determining which cells will synchronize. We remark that for  $r_0 = 0.25$  and  $r_0 = 0.5$ , where all the cells are much more closely spaced, asynchronous oscillations do not occur when  $\kappa = 45$ .

Lastly, we present global bifurcation diagrams versus  $D_0$  in the top panel of Fig. 20 that compares results for the leading-order dynamics, for symmetrically-spaced cells on a ring of radius  $r_0 = 0.25$ , and for arbitrarily located cells on a ring of radius  $r_0 = 0.25$ , as computed from (3.2), (4.5) and (4.14), respectively. We observe that the range of  $D_0$  for which linearly stable periodic solutions exist when the cells are arbitrarily located on the ring is only slightly larger than that of symmetric cells. This is likely due to the closer spatial proximity of some cells in this configuration relative to the symmetric cell pattern. For both configurations, when  $D_0$  is large, the bulk species diffuses away from the cells making it difficult for the cells to communicate. In the bottom panel of Fig. 20, we plot the HB bifurcation curves for  $r_0$  versus  $D_0$  for the arbitrarily-spaced configuration.

#### 4.3. Arbitrarily located cells within the unit sphere

In this subsection we consider  $m = 6$  identical cells that are arbitrarily located within the unit sphere, such as shown Fig. 21. The centers of the cells are chosen as in Table 3, and the common cell radius is  $\varepsilon = 0.05$ . For this cell configuration, we use the ODE system (4.14) to

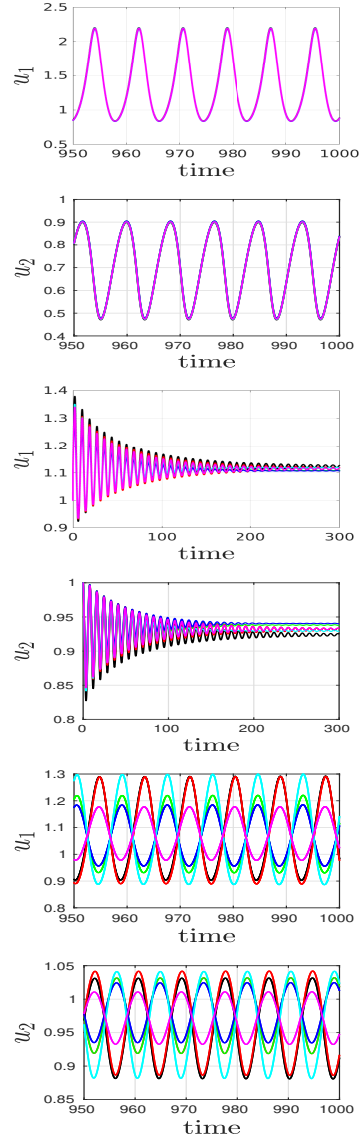
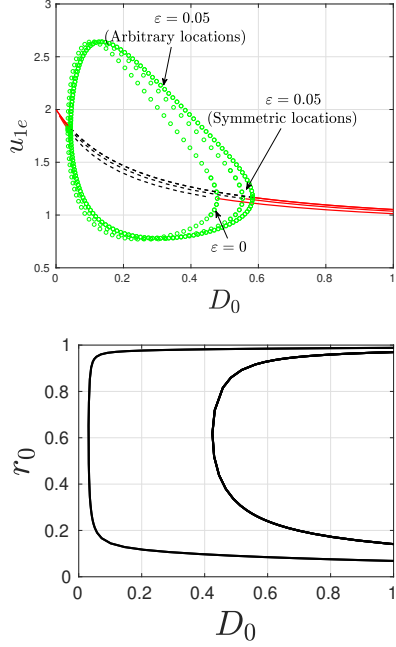


Figure 19: Numerical simulations of ODE dynamics for (4.14) computed using MATLAB for the parameters in the caption of Fig. 18 for arbitrarily-spaced cells on a concentric ring of radius  $r_0 = 0.85$  within the unit disk. Top rows: For  $\kappa = 5$ , sustained synchronous oscillations occur for the entire population. Middle rows: For  $\kappa = 25$ , decaying oscillations occur. Bottom rows: For  $\kappa = 45$ , asynchronous oscillations for two groups of cells that are the most closely spaced. The color codes of the trajectories correspond to the color codes for the cells in Fig. 14. The cell-cell distances are given in Table 2.

compute global bifurcation diagrams and we will calculate the Kuramoto order parameter (3.14) to study diffusion-mediated synchronization in the cells as  $D_0$  is increased.

For this cell configuration, in Fig. 22 we plot global bi-



*Figure 20:* Top panel: Global bifurcation diagrams for the ODE system (4.14) versus  $D_0$  for  $\kappa = 18.5$ , comparing results for the leading-order dynamics, for symmetrically-spaced cells on a ring, and for arbitrarily-spaced cells on a ring, as computed using MATCONT [29]. The ring radius is  $r_0 = 0.25$ , and the cell radius is  $\varepsilon = 0.05$ . Bottom panel: Two-parameter HB continuation for  $r_0$  versus  $D_0$  for arbitrarily-spaced cells on a ring. The horizontal line near  $r_0 = 1$  is beyond the range where the well-separated cell assumption is valid.

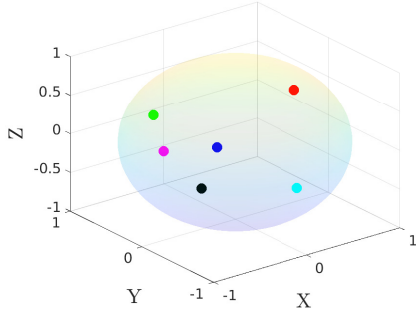


*Figure 21:* A schematic illustration for  $m = 6$  identical cells arbitrarily located within the unit sphere. The centers of the cells are given in Table 3. The color codes are for easy referencing.

furcation diagrams versus  $\kappa$  (top panel) and versus  $D_0$  (bottom panel) as computed from (4.14) using MATCONT [29]. In the top panel of Fig. 22 where  $D_0 = 0.5$ , the HB points are  $\kappa_1 = 1.5521$  and  $\kappa_2 = 15.2509$ , while for the bottom panel where  $\kappa = 3.2$  the HB occurs when  $D_0 = 0.0310$ . In this case, we observe that linearly stable periodic solutions exist for all  $D_0 \geq 0.0310$ .

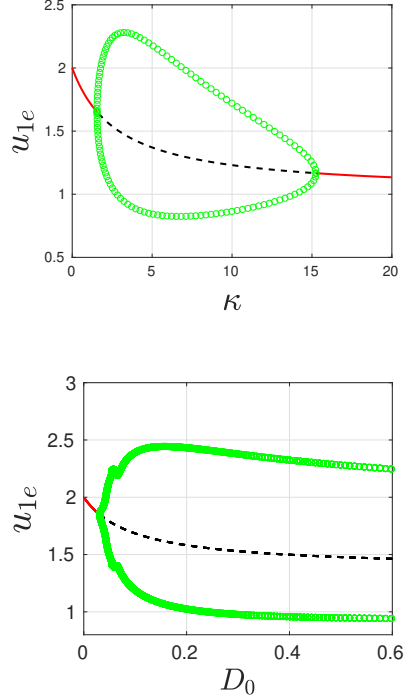


*Figure 22:* Global bifurcation diagrams versus  $\kappa$  (top panel) or versus  $D_0$  (bottom panel) for the ODE system (4.14) computed using MATCONT for  $m = 6$  identical cells arbitrarily located inside the unit sphere, with cell centers given in Table 3 (see Fig. 21) and with cell radius  $\varepsilon = 0.05$ . Top panel: For  $D_0 = 0.5$ , the HB points are at  $\kappa_1 = 1.5521$  and  $\kappa_2 = 15.2509$ . Bottom panel: For  $\kappa = 3.2$ , the unique HB point is  $D_0 = 0.0320$ . We predict that intracellular oscillations now occur for all  $D_0 > 0.03$ , and so will exist in the completely well-mixed regime where  $D_0 \rightarrow \infty$ .

To further investigate the effect of diffusion on the intracellular dynamics, in the top panel of Fig. 23 we show numerical results for the Kuramoto order parameter  $R$  (3.14) that measures the degree of phase synchronization of intracellular dynamics as  $D_0$  increases. In the bottom panel of Fig. 23 we also show the amplitude of oscillations in the cells and in the bulk region versus  $D_0$ . From the top panel of Fig. 23 we observe that there are no intracellular oscillations when  $D_0 \leq 0.0301$ , but that phase synchronization becomes more evident as  $D_0$  increases past  $D_0 = 0.0301$ , with almost perfect phase synchronization achieved when  $D_0 \approx 0.1$ .

These results illustrate *diffusion-mediated synchronization*, where an increase in the diffusion rate of the bulk species increases synchronization in the dynamics of the cells. We now verify our prediction from numerical simulations of the ODE system (4.14) for the cell configuration shown in Fig. 21. The results for  $u_{j1}$  are shown in

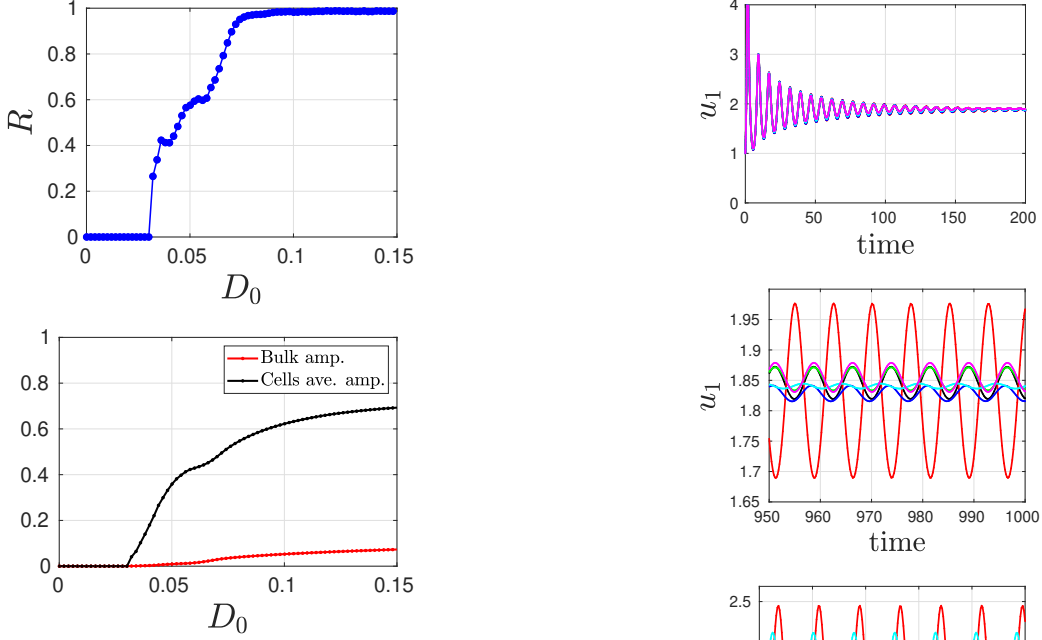


Figure 23: The degree of phase synchronization for  $m = 6$  identical cells of radius  $\varepsilon = 0.05$  arbitrarily located inside the unit sphere as shown in Fig. 21, computed using the ODEs (4.14) with  $\kappa = 3.2$ . Top panel: The Kuramoto order parameter  $R$  (3.14) versus  $D_0$ . Oscillations are triggered at  $D_0 \approx 0.0301$  and perfect phase synchronization is achieved at  $D_0 \approx 0.1$ . Bottom panel: Average amplitude of oscillation in the cells (black) and in the bulk region (red) versus  $D_0$ .

Fig. 24 for  $D_0 = 0.02$  (top row),  $D_0 = 0.0320$  (second row),  $D_0 = 0.0654$  (third row), and  $D_0 = 0.1348$  (fourth row). As predicted by the Kuramoto order parameter in Fig. 23, there are no sustained oscillations in the cells for  $D_0 = 0.02$ . For  $D_0 = 0.0320$  (second row), the cells begin to oscillate with only those that are in close spatial proximity beginning to synchronizing their dynamics, but with small amplitudes. As  $D_0$  increases further, phase synchronization becomes evident as shown in the third row where  $D_0 = 0.0654$ . The last row of Fig. 24 where  $D_0 = 0.1348$  shows perfect phase synchronization in the intracellular dynamics.

## 5. Instability triggered by a single cell

In this section, we study quorum-sensing (QS) behavior where a single additional cell is able to trigger intracellular oscillations for an entire collection of cells that would otherwise be in a quiescent state. For the three configurations of  $m = 6$  identical cells in the unit sphere considered in § 4, we introduce an additional cell centered at  $(0.75, 0, 0)$  and compare the global bifurcation diagrams for  $m = 6$  and  $m = 7$  identical cells. To es-

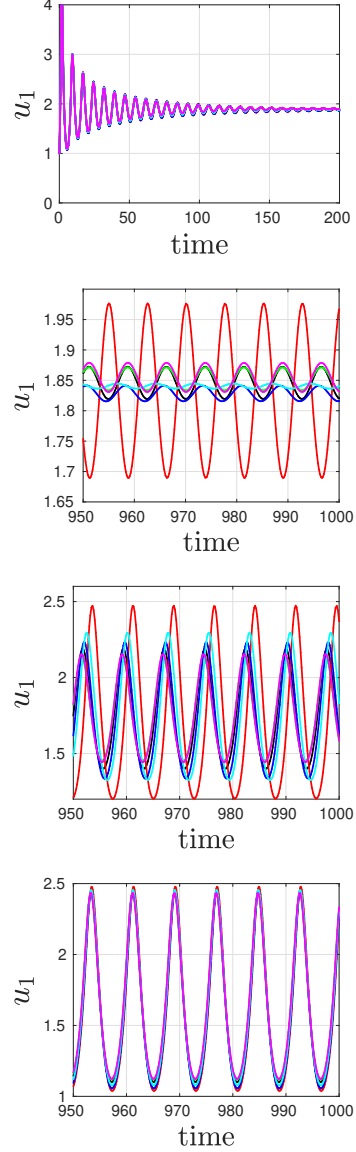


Figure 24: Numerical simulations of the ODE system (4.14) showing the intracellular species  $u_{j1}$  as computed using MATLAB for  $m = 6$  identical cells of radius  $\varepsilon = 0.05$ , arbitrarily located inside the unit sphere as shown in Fig. 21 with  $\kappa = 3.2$ . Row 1:  $D_0 = 0.02$ , Row 2:  $D_0 = 0.0320$ , Row 3:  $D_0 = 0.0654$ , and Row 4:  $D_0 = 0.1348$  where almost perfect phase synchrony occurs. Colors correspond to the color codes for the cells in Fig. 21.

tablish QS behavior, we seek parameter regimes where linearly stable periodic solutions exist for  $m = 7$  cells, but not for  $m = 6$  cells. In contrast to the typical study of QS behavior from ODEs in the well-mixed limit where spatial effects are neglected, our results below shows that the range of  $\kappa$  where QS occurs is dependent on the specific cell configuration used in § 4. The bifur-

608 cation results below are computed from the ODE system  
 609 (2.18) using MATCONT [29] for the Sel'kov parameters in (3.13) and with  $\rho = 1.4324$ ,  $D_0 = 0.5$ , and  
 610  $\varepsilon = 0.05$ .  
 611

612 We first consider the symmetrically-spaced cell configura-  
 613 tion with ring radius  $r_0 = 0.5$ , where the updated  
 614 configuration that includes the seventh cell (in orange)  
 615 is shown in the top row of Fig. 25. In the second row of  
 616 Fig. 25 we show the global bifurcation diagrams versus  
 617 the bulk decay rate  $\kappa$  for either  $m = 6$  or  $m = 7$  identi-  
 618 cal cells. From this figure, we observe that on the range  
 619  $13.5721 < \kappa < 16.9869$  collective intracellular oscilla-  
 620 tions will occur only when the seventh cell is added. To  
 621 further illustrate this QS behavior, we compute the time-  
 622 dependent dynamics of  $u_{j1}(t)$  from the ODEs (2.18) for  
 623  $m = 6$  and  $m = 7$  cells with  $\kappa = 16$ , as shown in the third  
 624 and fourth rows of Fig. 25, respectively. For  $m = 6$ , we  
 625 observe, as expected, a slow synchronous decay of the  
 626 intracellular oscillations to their common steady-state  
 627 limit. However, by introducing the additional cell, we  
 628 observe from the fourth row of Fig. 25 sustained, nearly  
 629 synchronous, intracellular oscillations of different am-  
 630 plitudes. In particular, the cell closest to the seventh  
 631 (orange) cell is the black cell centered at  $(0.5, 0, 0)$ . We  
 632 observe that among all the cells, these two cells have the  
 633 largest amplitude of oscillations.

634 A similar result is shown in Fig. 26 for  $m = 7$  identi-  
 635 cal cells, where six of the cells are arbitrarily located  
 636 on a ring of radius  $r_0 = 0.5$ , where the coordinates of  
 637 the cell centers are in Table 1. The cell configuration is  
 638 shown in the top row of Fig. 26. From the global bifur-  
 639 cation diagrams shown in the second row of Fig. 26, for  
 640 the range  $14.0392 < \kappa < 17.4189$  collective intracel-  
 641 lular oscillations will occur only when the seventh cell  
 642 is added. For  $\kappa = 17$ , the trajectories for  $u_{j1}(t)$  com-  
 643 puted from the ODEs (2.18) for  $m = 6$  and  $m = 7$  cells  
 644 are shown in the third and fourth rows of Fig. 26, re-  
 645 spectively. For this cell configuration, we observe that  
 646 it is now the green cell that is closest to the seventh (or-  
 647 ange) cell. From the fourth row of Fig. 26, we observe  
 648 that these two cells oscillate in near synchrony and they  
 649 have the largest amplitudes of oscillation.

650 Finally, we assume that the six cells are arbitrarily lo-  
 651 cated inside the unit sphere as shown in the top row  
 652 of Fig. 27. The centers of the first six cells, their dis-  
 653 tances from the origin, and their center-to-center dis-  
 654 tances are as in Tables 3 and 4, respectively. Based on  
 655 the global bifurcation diagrams shown in the second row  
 656 of Fig. 27, on the range  $15.2509 < \kappa < 17.41885$  col-  
 657 lective intracellular oscillations will occur only when the

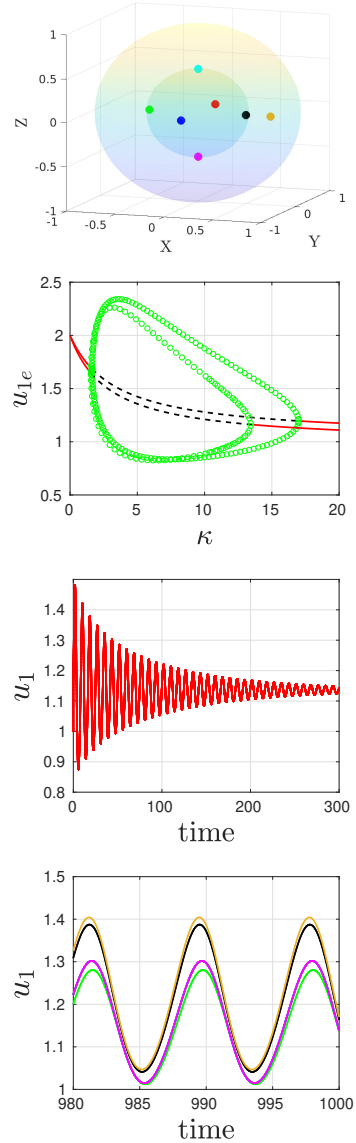


Figure 25: Global bifurcation diagram and numerical results for  $u_{j1}$  from the ODE system (2.18) computed using MATLAB for  $m = 6$  and  $m = 7$  identical cells of radius  $\varepsilon = 0.05$  and with  $D_0 = 0.5$ . Top row: Schematic diagram showing the locations of the cells, where the first six cells are symmetrically placed on a concentric sphere of radius  $r_0 = 0.5$  (see Fig. 7 for the centers of the cells) and the seventh cell is located at  $(0.75, 0, 0)$ . Second row: Global bifurcation diagram for the first six cells only (inner loop) with HB points at  $\kappa_1 = 1.5504$  and  $\kappa_2 = 13.5721$ , and for all the seven cells (outer loop) with HB points at  $\kappa_1 = 1.6465$  and  $\kappa_2 = 16.9869$ . Third Row: Numerical simulations for  $u_{j1}$  from the ODE system (2.18) for the first six cells only for  $\kappa = 16$ , showing decaying oscillations. Bottom row: For  $\kappa = 16$ , by including the seventh cell, sustained nearly synchronous oscillations will occur. The colors of the trajectories correspond to the color codes for the cells in the top row.

658 seventh cell is added. The numerical results for the tra-  
 659 jectories  $u_{j1}(t)$  computed from the ODEs (2.18) when  
 660  $\kappa = 17$ , as shown in the third and fourth rows of Fig. 27,  
 661 confirm this predicted QS behavior.

662 Overall, these results show that the inclusion of one sin-  
 663 gle additional cell can, in some parameter range of  $\kappa$ ,  
 664 trigger intracellular oscillations in the entire collection  
 665 of cells that otherwise would not occur. Moreover, we  
 666 emphasize that the ranges of  $\kappa$  where this QS behavior  
 667 will occur depends on the particular spatial configura-  
 668 tion of cells. This additional qualitative feature that ac-  
 669 counts for the effect of spatial heterogeneity results from  
 670 the Neumann Green's matrix in (2.18).

## 671 6. An integro-differential system for $D = O(1)$

672 In the limit  $\varepsilon \rightarrow 0$ , we asymptotically reduce (1.2) to de-  
 673 rive an integro-differential ODE system for the intracel-  
 674 lular dynamics  $\mathbf{u}_j(t)$ , which is valid when  $D = O(1)$ . For  
 675  $D = O(1)$ , the limiting bulk diffusion field is no longer  
 676 approximately spatially homogeneous, and so the previ-  
 677 ous analysis in §2 is no longer valid. For simplicity, in  
 678 the analysis below we will assume that the initial con-  
 679 ditions are  $\mathbf{u}_j(0) = 0$  and that  $U(\mathbf{x}, 0) = 0$ .

Since there is no initial transient near the cells, we can use the quasi-steady approximation near the cells for all  $t > 0$ . In this way, for  $t = O(1)$ , in the  $j^{\text{th}}$  inner region we introduce the local variables  $\mathbf{y} = \varepsilon^{-1}(\mathbf{x} - \mathbf{x}_j)$ ,  $\rho = |\mathbf{y}|$ , and  $V_j(\mathbf{y}, t) = U(\mathbf{x}_j + \varepsilon\mathbf{y}, t)$ . From (1.2a) and (1.2c), we get the leading-order quasi-steady problem

$$\begin{aligned} \Delta_{\mathbf{y}} V_j &= 0, \quad \text{for } \rho > 1, \\ D\partial_{\rho} V_j &= d_{1j}V - \frac{d_{2j}}{\varepsilon}u_{j1}, \quad \text{on } \rho = 1, \end{aligned} \quad (6.1)$$

which has the radially symmetric solution

$$V(\mathbf{y}, t) = \frac{A_j}{\rho} + B_j, \quad A_j = \frac{\gamma_j}{4\pi\varepsilon D} \left( u_{j1} - \frac{\varepsilon d_{1j}}{d_{2j}} B_j \right), \quad (6.2)$$

where  $A_j \equiv A_j(t)$ ,  $B_j \equiv B_j(t)$  and  $u_{j1} \equiv u_{j1}(t)$ , with initial values  $A_j(0) = B_j(0) = u_{j1}(0) = 0$ . Here  $\gamma_j$  is

$$\gamma_j \equiv \frac{4\pi D d_{2j}}{d_{1j} + D}. \quad (6.3)$$

By substituting (6.2) into the intracellular dynamics (1.2d) we obtain the following ODE that is coupled to  $B_j$  for each  $j = 1, \dots, m$ :

$$\frac{du_j}{dt} = \mathbf{F}_j(\mathbf{u}_j) - \gamma_j u_{j1} \mathbf{e}_1 + \frac{\varepsilon d_{1j}}{d_{2j}} \gamma_j B_j(t) \mathbf{e}_1. \quad (6.4)$$

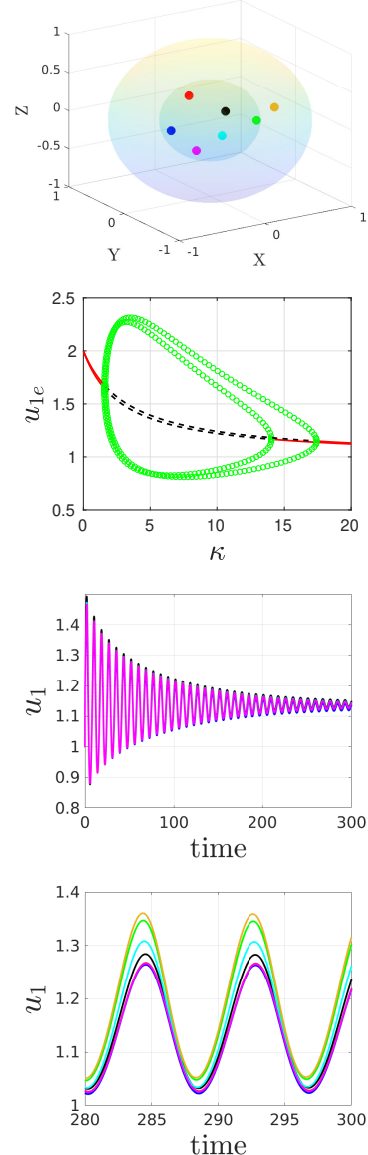


Figure 26: Same caption in Fig. 25 except that the first six cells are arbitrarily-spaced on a concentric sphere of radius  $r_0 = 0.5$  (see Table 1 for the centers of the cells), with the seventh cell located at  $(0.75, 0, 0)$ . Top row: Schematic diagram showing the locations of the cells. Second row: Global bifurcation diagram for the first six cells only (inner loop) with HB points at  $\kappa_1 = 1.5504$  and  $\kappa_2 = 14.0392$ , and for all the seven cells (outer loop) with HB points at  $\kappa_1 = 1.6460$  and  $\kappa_2 = 17.4189$ . Numerical results for  $u_{j1}(t)$  from the ODE system (2.18) when  $\kappa = 17$  for the first six cells (third row) only and by including the seventh cell (bottom row). We observe that the inclusion of the seventh cell triggers sustained, and nearly synchronous, oscillations in all of the cells. The colors of the trajectories coincide with the color codes of the cells in the top row.

To determine  $B_j(t)$  we must match the inner solution near the cells to an outer bulk solution. Upon writing

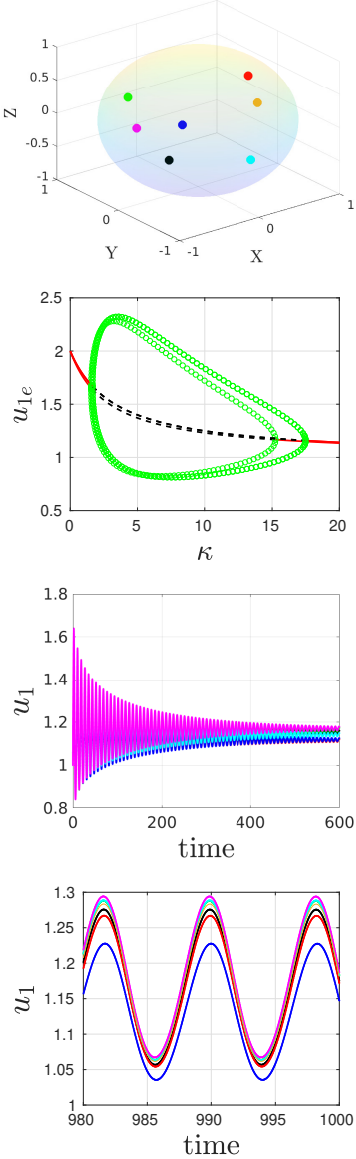


Figure 27: Same caption in Fig. 25 except that the first six cells are arbitrarily spaced within the unit sphere (see Table 3 for the centers of the cells), with the seventh cell located at \$(0.75, 0, 0)\$. Top row: Schematic diagram showing the cell locations. Second row: Global bifurcation diagram for the first six cells only (inner loop) with HB points at \$\kappa\_1 = 1.5521\$ and \$\kappa\_2 = 15.2509\$, and for all the seven cells (outer loop) with HB points at \$\kappa\_1 = 1.6453\$ and \$\kappa\_2 = 17.4885\$. Numerical results for \$u\_{jl}(t)\$ from the ODE system (2.18) when \$\kappa = 17\$ for the first six cells (third row) only and by including the seventh cell (bottom row). Once again, the seventh cell triggers sustained, and nearly synchronous, oscillations in all of the cells. The colors of the trajectories coincide with the color codes of the cells in the top row.

(6.2) in outer variables by using \$\varepsilon\rho = |\mathbf{x} - \mathbf{x}\_j|\$, we obtain

that the outer bulk solution \$U(\mathbf{x}, t)\$ satisfies

$$\begin{aligned} U_t &= D\Delta U - \kappa U, \quad \mathbf{x} \in \Omega \setminus \{\mathbf{x}_1, \dots, \mathbf{x}_m\}; \quad U(\mathbf{x}; 0) = 0, \\ U &\sim \frac{\varepsilon A_j}{|\mathbf{x} - \mathbf{x}_j|} + B_j + o(1), \quad \text{as } \mathbf{x} \rightarrow \mathbf{x}_j, \quad j = 1, \dots, m, \\ \partial_n U &= 0, \quad \mathbf{x} \in \partial\Omega. \end{aligned} \quad (6.5)$$

To solve (6.5), we first take the Laplace transform to derive that \$\hat{U}(\mathbf{x}, s) = \mathcal{L}[U(\mathbf{x}, t)]\$ satisfies

$$\begin{aligned} \Delta \hat{U} - \frac{(\kappa + s)}{D} \hat{U} &= -4\pi\varepsilon \sum_{k=1}^N \hat{A}_k \delta(\mathbf{x} - \mathbf{x}_k), \quad \mathbf{x} \in \Omega, \\ \hat{U} &\sim \frac{\varepsilon \hat{A}_j}{|\mathbf{x} - \mathbf{x}_j|} + \hat{B}_j, \quad \text{as } \mathbf{x} \rightarrow \mathbf{x}_j, \quad j = 1, \dots, m, \\ \partial_n \hat{U} &= 0, \quad \mathbf{x} \in \partial\Omega, \end{aligned} \quad (6.6)$$

where \$\hat{A}\_j = \mathcal{L}[A\_j(t)]\$ and \$\hat{B}\_j = \mathcal{L}[B\_j(t)]\$.

Next, we decompose (6.6) by writing

$$\hat{U}(\mathbf{x}, s) = 4\pi\varepsilon \sum_{k=1}^N \hat{A}_k \hat{G}(\mathbf{x}, s; \mathbf{x}_k), \quad (6.7)$$

where \$\hat{G}(\mathbf{x}, s; \mathbf{x}\_k)\$ is the Green's function satisfying

$$\begin{aligned} \Delta \hat{G} - \frac{(\kappa + s)}{D} \hat{G} &= -\delta(\mathbf{x} - \mathbf{x}_k), \quad \mathbf{x} \in \Omega, \\ \hat{G} &\sim \frac{1}{4\pi|\mathbf{x} - \mathbf{x}_k|} + \hat{R}_k + o(1), \quad \text{as } \mathbf{x} \rightarrow \mathbf{x}_k, \\ \partial_n \hat{G} &= 0, \quad \mathbf{x} \in \partial\Omega, \end{aligned} \quad (6.8)$$

where \$\hat{R}\_k(s)\$ is the regular part of \$\hat{G}\$, which depends on \$\mathbf{x}\_k\$. It readily follows that the inverse Laplace transform is

$$G_h(\mathbf{x}, t; \mathbf{x}_k) = D^{-1} \mathcal{L}^{-1} [\hat{G}(\mathbf{x}, s; \mathbf{x}_k)], \quad (6.9)$$

where \$G\_h(\mathbf{x}, t; \mathbf{x}\_k)\$ is the heat kernel for \$\Omega\$ defined by the solution to

$$\begin{aligned} \partial_t G_h &= D\Delta G_h - \kappa G_h, \quad \mathbf{x} \in \Omega, \\ G_h(\mathbf{x}, 0; \mathbf{x}_k) &= \delta(\mathbf{x} - \mathbf{x}_k); \quad \partial_n G_h = 0, \quad \mathbf{x} \in \partial\Omega. \end{aligned} \quad (6.10)$$

We remark that for the unit sphere, \$\hat{G}\$ and \$\hat{R}\_k\$ can be determined analytically as (see equations (3.13) and (3.14) of [33])

$$\hat{G}(\mathbf{x}, s; \mathbf{x}_k) = \frac{e^{-\alpha|\mathbf{x} - \mathbf{x}_k|}}{4\pi|\mathbf{x} - \mathbf{x}_k|} + \hat{G}_p(\mathbf{x}, s; \mathbf{x}_k), \quad (6.11a)$$

where  $\alpha \equiv \sqrt{(s + \kappa)/D}$  is the principal branch of the square root and where

$$\hat{G}_p = \sum_{n=0}^{\infty} \frac{(2n+1)\beta_n}{4\pi \sqrt{|\mathbf{x}||\mathbf{x}_k|}} P_n(\cos \omega) I_{n+1/2}(\alpha|\mathbf{x}|) I_{n+1/2}(\alpha|\mathbf{x}_k|). \quad (6.11b)$$

In (6.11b),  $\cos(\omega)$  and the coefficients  $\beta_n$  are defined by

$$\cos(\omega) = \frac{\mathbf{x} \cdot \mathbf{x}_k}{|\mathbf{x}||\mathbf{x}_k|}, \quad \beta_n \equiv \frac{\alpha K_{n+3/2}(\alpha) - n K_{n+1/2}(\alpha)}{\alpha I_{n+3/2}(\alpha) + n I_{n+1/2}(\alpha)}, \quad (6.11c)$$

$P_n(z)$  are Legendre polynomials, and  $I_{n+1/2}(z)$  and  $K_{n+1/2}(z)$  are modified Bessel functions of the first and second kind. By letting  $\mathbf{x} \rightarrow \mathbf{x}_k$  in (6.11), we use  $P_n(1) = 1$  to identify the regular part in (6.8) as

$$\hat{R}_k(s) = -\frac{\alpha}{4\pi} + \frac{1}{4\pi|\mathbf{x}_k|} \sum_{n=0}^{\infty} (2n+1)\beta_n [I_{n+1/2}(\alpha|\mathbf{x}_k|)]^2. \quad (6.12)$$

Next, by letting  $\mathbf{x} \rightarrow \mathbf{x}_j$  in (6.7) we enforce that the limiting behavior agrees with that required in (6.6). This yields for each  $j = 1, \dots, m$  that

$$4\pi\varepsilon \left[ \hat{A}_j(s)\hat{R}_j(s) + \sum_{k \neq j}^m \hat{A}_k(s)\hat{G}(\mathbf{x}_j, s; \mathbf{x}_k) \right] = \hat{B}_j(s). \quad (6.13)$$

Upon using  $\hat{A}_j \sim \gamma_j \hat{u}_{j1}(s)/(4\pi\varepsilon D) + O(\varepsilon)$  from (6.2), we obtain that

$$\hat{B}_j(s) \sim \frac{\gamma_j}{D} \hat{u}_{j1}(s)\hat{R}_j(s) + \sum_{k \neq j}^m \frac{\gamma_k}{D} \hat{u}_{k1}(s)\hat{G}(\mathbf{x}_j, s; \mathbf{x}_k) + O(\varepsilon). \quad (6.14)$$

Finally, we invert the Laplace transform using (6.9) and the convolution property to obtain for  $j = 1, \dots, m$  that

$$\begin{aligned} B_j(t) &= \frac{\gamma_j}{D} \int_0^t u_{j1}(\tau) R_j(t-\tau) d\tau \\ &\quad + \sum_{k \neq j}^m \gamma_k \int_0^t u_{k1}(\tau) G_h(\mathbf{x}_j, t-\tau, \mathbf{x}_k) d\tau, \end{aligned} \quad (6.15)$$

where  $R_j(t) = \mathcal{L}^{-1}[\hat{R}_j(s)]$ . The integro-differential system for the intracellular kinetics  $\mathbf{u}_j(t)$ , with initial value  $\mathbf{u}_j(0) = 0$ , is obtained by substituting (6.15) into (6.4).

We emphasize that for the sphere, where analytical formulae for the Laplace transforms of  $R_j(t)$  and  $G_h(\mathbf{x}_j, t, \mathbf{x}_k)$  are available (see (6.11) and (6.12)), it should be possible to use the *sum-of-exponentials* (cf. [34], [35], [36]) approximation in the Laplace transform plane for the convolution kernels in (6.15) in order to develop a time-marching scheme for the intracellular dynamics. This is the topic of ongoing work.

## 7. Discussion

We have extended the coupled 2-D cell-bulk ODE-PDE model of [18, 23, 24] to a 3-D bounded domain, where the cells are small spheres of a common radius that are spatially segregated within the domain. Our model is related to the 3-D cell-bulk model formulated in [19, 20, 25] in all of  $\mathbb{R}^3$ , where there was a single intracellular species within each cell and where the bulk medium was purely diffusive. In a bounded 3-D domain, and in the limit of large bulk diffusivity  $D = D_0/\varepsilon$ , where  $D_0 = O(1)$  and  $\varepsilon \ll 1$ , the method of matched asymptotic analysis was used to reduce the cell-bulk ODE-PDE model to a novel ODE system for the average bulk chemical concentration that still retains the diffusion parameter  $D_0$  and an  $O(\varepsilon)$  correction term that depends on the spatial configuration of the cells through the Neumann Green's matrix. For a spherical domain, where this Green's matrix can be evaluated analytically, and for two-component Sel'kov-type intracellular reaction-kinetics we showed from our ODE system that both quorum-sensing and diffusion-mediated communication can occur. We emphasize that our new ODE system is distinct from the type of ODE system with global coupling that is usually formulated in the well-mixed limit  $D \rightarrow \infty$  to study quorum-sensing behavior, where spatial heterogeneity is neglected and there is no diffusivity parameter.

For the leading-order dynamics of our ODE system, where the spatial configuration of cells is neglected, we used the Kuramoto order parameter to study the degree of phase synchronization in the intracellular dynamics as a cell density parameter  $\rho = m/|\Omega|$  increases for a fixed population of  $m = 1000$  cells. The cell population was composed of two groups: identical cells and *defective* cells, the latter of which have a random parameter in the Sel'kov reaction kinetics. For all the scenarios considered, and as similar to the results in section 4.2 of [24], the cell density parameter was shown to play a dual role of both triggering and quenching intracellular oscillations. Synchronous oscillations are triggered through quorum sensing when the cell density crosses a specific threshold, and are extinguished when the cell density parameter exceeds a further threshold. The QS behavior observed here leads to a roughly switch-like transition of the cells from a quiescent state to perfect phase synchronization. The range of  $\rho$  where nearly perfect phase synchronization occurs was shown to decrease as the heterogeneity in the cell population increases. This illustrates, as expected, that it is more difficult to trigger intracellular oscillations for a population of non-identical cells.

743 Furthermore, we studied the effect of the spatial config-  
 744 uration of the cells on their intracellular dynamics by  
 745 including the  $O(\varepsilon)$  correction terms of the novel ODE  
 746 system (2.18) in our analysis. These correction terms  
 747 incorporate the spatial locations of the cells into the  
 748 ODE system. Their coefficients can be rather signif-  
 749 icant even for moderately small values of  $\varepsilon$  and, as a  
 750 result, we showed that they played an important role in  
 751 studying quorum-sensing and diffusion-mediated inter-  
 752 cellular communication.

753 There are several possible extensions of the modeling  
 754 framework and analysis provided in this paper. Firstly,  
 755 for our novel ODE system, which incorporates weak  
 756 spatial heterogeneity, it would be interesting to consider  
 757 the influence of a single defective cell on a population  
 758 of identical cells, similar to that studied for the 2-D  
 759 problem in [23, 24]. In particular, can a single defec-  
 760 tive cell either extinguish or trigger intracellular oscil-  
 761 lations in the entire group of cells? Secondly, the de-  
 762 velopment of a viable numerical approach to numeri-  
 763 cally solve the 3-D cell-bulk model, in order to con-  
 764 firm the asymptotic results, should be undertaken. This  
 765 validation was done for the 2-D case in [23] using the  
 766 commercial solver *FLEXPDE*, but the 3-D problem is  
 767 more challenging. Thirdly, for the regime of finite diffu-  
 768 sion where  $D = O(1)$  it would be worthwhile to extend  
 769 the time-marching approach developed in [37] for the  
 770 integro-differential ODE system for the cell-bulk model  
 771 in  $\mathbb{R}^2$  to our 3-D setting. In particular, by using the *sum-*  
 772 *of-exponentials* approximation together with Duhamel's  
 773 integral, it should be possible to develop an accurate  
 774 time-marching scheme to numerically solve the integro-  
 775 differential system (6.15) and (6.4). Without such an  
 776 approach, it is computationally very inefficient to nu-  
 777 mERICALLY solve (6.15) and (6.4) with a standard time-  
 778 discretization since  $O(m^2)$  convolution integrals with  
 779 full memory dependence would have to be evaluated  
 780 at time  $t$  to advance the solution one time-step to time  
 781  $t + \Delta t$ . Moreover, the convolution integrals in (6.15) are  
 782 improper integrals that need a careful analysis, where  
 783 the local behavior near the integrable singularity is ap-  
 784 proximated analytically. The approach used in [37] for  
 785 the analogous 2-D cell-bulk model in  $\mathbb{R}^2$  overcame both  
 786 of these challenges.

787 Finally, throughout this paper, we used the Sel'kov-type  
 788 kinetics in [27] as a prototypical conditional oscillator  
 789 to investigate intracellular oscillations for our 3-D cell-  
 790 bulk model. An interesting future direction would be to  
 791 apply our theoretical approach for a biologically moti-  
 792 vated intracellular kinetics such as those in [9, 38] used  
 793 to model glycolytic oscillations in yeast cells or the *Lux*

794 kinetics used to model bioluminescence behavior [8].

## 795 Acknowledgments

796 Michael J. Ward gratefully acknowledges the support of  
 797 the NSERC Discovery Grant Program.

# 798 Appendices

## 799 A. Non-dimensionalization of the cell-bulk model

In this appendix we non-dimensionalize the cell-bulk (1.1) into its dimensionless form in (1.2). The dimensions, labeled by [...], of the quantities in (1.1) are

$$[\mathcal{U}] = \frac{\text{moles}}{\text{length}^3}, \quad [D_B] = \frac{\text{length}^2}{\text{time}}, \quad [\mu_j] = [\mu_c] = \frac{\text{moles}}{\text{length}^3},$$

$$[k_R] = [k_B] = \frac{1}{\text{time}}, \quad [\mathbf{X}] = \text{length} \quad [T] = \text{time},$$

$$[\beta_{1j}] = \frac{\text{length}}{\text{time}}, \quad [\beta_{2j}] = \frac{1}{\text{time} \times \text{length}^2}.$$

We assume that the common radius  $R$  of the cells  $\Omega_j$  for  $j = 1, \dots, m$  is small compared to the length-scale  $L$  of  $\Omega$ , and so we introduce a small parameter  $\varepsilon \equiv R/L \ll 1$ . In addition, we introduce the  $t$ ,  $\mathbf{x}$ ,  $U$  and  $\mathbf{u}$  by

$$U = \frac{L^3}{\mu_c} \mathcal{U}, \quad \mathbf{x} = \frac{\mathbf{X}}{L}, \quad t = k_R T, \quad \mathbf{u}_j = \frac{\mu_j}{\mu_c} \mathbf{u}, \quad (\text{A.1})$$

so that the time-scale is chosen based on the reaction kinetics. We find that the dimensionless bulk diffusion field satisfies (1.2a), while on the cell boundary (1.1c) becomes

$$D \partial_{n_x} U = \frac{\beta_{1j}}{Lk_R} U - \frac{\beta_{2j} L^2}{k_R} u_{j1}, \quad \mathbf{x} \in \partial\Omega_{\varepsilon_j}. \quad (\text{A.2})$$

Similarly, by using  $dS_{\mathbf{x}} = L^2 dS_x$ , the dimensional intracellular kinetics (1.1d) transforms to

$$\frac{d\mathbf{u}_j}{dt} = \mathbf{F}_j(\mathbf{u}_j) + \mathbf{e}_1 \int_{\partial\Omega_{\varepsilon_j}} \left( \frac{\beta_{1j}}{Lk_R} - \frac{L^2 \beta_{2j}}{k_R} u_{j1} \right) dS_{\mathbf{x}}, \quad (\text{A.3})$$

where  $\partial\Omega_{\varepsilon_j}$  is the surface of a sphere of radius  $\varepsilon$ . Since  $|\partial\Omega_{\varepsilon_j}| = O(\varepsilon^2)$ , in order to ensure that there is an  $O(1)$  efflux out of the  $j^{\text{th}}$  cell into the bulk medium, we must consider the limit where  $\beta_{2j} L^2 / k_R = O(\varepsilon^{-2})$ . Moreover, the feedback into the  $j^{\text{th}}$  cell from the bulk is  $O(\varepsilon)$  when the dimensionless influx parameter is on the asymptotic

806 range  $\beta_{1j}/(Lk_R) = O(\varepsilon^{-1})$ . Based on these observations,  
 807 we chose the permeability scalings as in (1.3). With  
 808 this choice, (A.2) and (A.3) become (1.2c) and (1.2d),  
 809 respectively.

## 810 B. Cell locations

811 Here, we give the coordinates of the centers of the cells  
 812 for the different configurations considered in this paper.

### 813 B.1. Arbitrarily located cells on a sphere of radius $r_0$

814 In Table 1 below, we give the coordinates of  $m = 6$   
 815 cells on the surface of the unit sphere (corresponding to  
 816  $r_0 = 1$ ). These coordinates can be used to generate the  
 817 centers of cells on any sphere of radius  $0 < r_0 < 1$  by  
 scaling appropriately.

Cell $i$	$x_i$	$y_i$	$z_i$	color code
1	-0.1639	-0.8138	0.5576	black
2	0.9691	-0.1934	-0.1531	green
3	-0.5636	-0.1124	0.8184	red
4	-0.4022	0.7875	-0.4671	blue
5	0.5681	0.4443	-0.6927	cyan
6	-0.6892	-0.5772	-0.4380	magenta

818  
 819 Table 1: Coordinates of the center of  $m = 6$  cells arbitrarily located  
 820 on the surface of the unit sphere. Colors corresponds to color codes  
 for the cells in Fig. 14.

821 In Table 2 we give the center-to-center distances be-  
 822 tween the cells with coordinates in Table 1.

### 823 B.2. Arbitrarily located cells inside the unit sphere

824 In Table 3 and Table 4 we give the coordinates of the  
 825 centers of  $m = 6$  identical cells arbitrarily located inside  
 the unit sphere, their distance from the origin, and their  
 center-to-center distances.

## 826 References

- [1] S. De Monte, F. d’Ovidio, S. Danø, P. Sørensen, Dynamical quorum sensing: Population density encoded in cellular dynamics, PNAS 104 (2007) 18377–18381.
- [2] S. Danø, P. Sørensen, F. Hynne, Sustained oscillations in living cells, Nature 402 (1999) 320–322.
- [3] S. Danø, P. Sørensen, et al., Quantitative characterization of cell synchronization in yeast, PNAS 104 (2007) 12732–12736.
- [4] T. Gregor, K. Fujimoto, N. Masaki, S. Sawai, The onset of collective behavior in social amoebae, Science 328 (2010) 1021–1025.
- [5] V. Nanjundiah, Cyclic amp oscillations in dictyostelium discoideum: models and observations, Biophys. Chem. 72 (1998) 1–8.
- [6] A. Goldbeter, Biochemical oscillations and cellular rhythms: the molecular bases of periodic and chaotic behaviour, Cambridge university press, 1997.
- [7] M. E. Taga, B. L. Bassler, Chemical communication among bacteria, PNAS 100 (2003) 14549–14554.
- [8] P. Melke, P. Sahlin, A. Levchenko, H. Jönsson, A cell-based model for quorum sensing in heterogeneous bacterial colonies, PLoS Comput. Biol. 6 (2010) e1000819.
- [9] P. Mina, M. di Bernardo, N. J. Savery, K. Tsaneva-Atanasova, Modelling emergence of oscillations in communicating bacteria: a structured approach from one to many cells, J. Royal Soc. Interface 10 (2013) 20120612.
- [10] K. Kamino, K. Fujimoto, S. Sawai, Collective oscillations in developing cells: Insights from simple systems, Development, growth & differentiation 53 (2011) 503–517.
- [11] M. R. Tinsley, A. F. Taylor, Z. Huang, F. Wang, K. Showalter, Dynamical quorum sensing and synchronization in collections of excitable and oscillatory catalytic particles, Physica D 239 (2010) 785–790.
- [12] M. R. Tinsley, A. F. Taylor, Z. Huang, K. Showalter, Emergence of collective behavior in groups of excitable catalyst-loaded particles: spatiotemporal dynamical quorum sensing, Phys. Rev. Lett. 102 (2009) 158301.
- [13] A. F. Taylor, M. R. Tinsley, K. Showalter, Insights into collective cell behaviour from populations of coupled chemical oscillators, Phys. Chem. Chem. Phys. 17 (2015) 20047–20055.
- [14] A. F. Taylor, M. R. Tinsley, F. Wang, Z. Huang, K. Showalter, Dynamical quorum sensing and synchronization in large populations of chemical oscillators, Science 323 (2009) 614–617.
- [15] J. D. Dockery, J. P. Keener, A mathematical model for quorum sensing in pseudomonas aeruginosa, Bull. Math. Biol. 63 (2001) 95–116.
- [16] J. P. Ward, J. R. King, A. J. Koerber, P. Williams, J. M. Croft, R. E. Sockett, Mathematical modelling of quorum sensing in bacteria, Math Medicine and Biol. 18 (2001) 263–292.
- [17] W. Ridgway, M. J. Ward, B. T. Wetton, Quorum-sensing induced transitions between bistable steady-states for a cell-bulk ODE-PDE model with Lux intracellular kinetics, J. Math. Bio. 84 (2021).
- [18] J. Gou, M. Ward, An asymptotic analysis of a 2-D model of dynamically active compartments coupled by bulk diffusion, J. Nonlin. Sci. 26 (2016) 979–1029.
- [19] J. Müller, C. Kuttler, B. A. Hense, M. Rothbauer, A. Hartmann, Cell-cell communication by quorum sensing and dimension-reduction, J. Math. Bio. 53 (2006) 672–702.
- [20] J. Müller, H. Uecker, Approximating the dynamics of communicating cells in a diffusive medium by ODEs—homogenization with localization, J. Math. Bio. 67 (2013) 1023–1065.
- [21] B. W. Li, C. Fu, H. Zhang, X. Wang, Synchronization and quorum sensing in an ensemble of indirectly coupled chaotic oscillators, Phys. Rev. E. 86 (2012) 046207.
- [22] B. W. Li, X. Z. Cao, C. Fu, Quorum sensing in populations of spatially extended chaotic oscillators coupled indirectly via a heterogeneous environment, J. Nonlin. Sci. 27 (2017) 1667–1686.
- [23] S. Iyaniwura, M. Ward, Synchrony and oscillatory dynamics for a 2-D PDE-ODE model of diffusion-sensing with small signaling compartments, SIAM J. Appl. Dyn. Sys. 20 (2021) 438–499.
- [24] S. Iyaniwura, M. J. Ward, Localized signaling compartments in 2-D coupled by a bulk diffusion field: Quorum sensing and synchronous oscillations in the well-mixed limit, Europ. J. Appl. Math. 32 (2021) 1001–1031.
- [25] H. Uecke, J. Müller, B. A. Hense, Individual-based model for quorum sensing with background flow, Bull. Math. Bio. 76 (2014) 1727–1746.

Cell color	Black	Green	Red	Blue	Cyan	Magenta
Black	0	1.474	0.848	1.916	1.919	1.150
Green	1.474	0	1.818	1.715	0.927	1.726
Red	0.848	1.817	0	1.578	1.968	1.346
Blue	1.916	1.715	1.578	0	1.054	1.395
Cyan	1.919	0.927	1.968	1.054	0	1.634
Magenta	1.150	1.726	1.346	1.395	1.634	0

Table 2: The center-to-center distance between the cells presented in Table 1 for  $r_0 = 0.85$ . Colors corresponds to color codes for the cells in Fig. 14.

Cell $i$	$x_i$	$y_i$	$z_i$	Distance from origin	Color code
1	-0.2336	0.1684	-0.6002	0.6657	black
2	-0.4370	0.5739	0.2368	0.7592	green
3	0.5784	-0.0731	0.5103	0.7748	red
4	-0.3054	-0.1425	0.0993	0.3513	blue
5	0.4521	-0.2760	-0.6256	0.8197	cyan
6	-0.4092	0.4664	-0.1933	0.6499	magenta

Table 3: Coordinates of the center of  $m = 6$  cells arbitrarily located inside the unit sphere, and their distances from the origin.

Cell color	Black	Green	Red	Blue	Cyan	Magenta
Black	0	0.9520	1.3967	0.7688	0.8175	0.5340
Green	0.9520	0	1.2347	0.7413	1.5022	0.4442
Red	1.3967	1.2347	0	0.9772	1.1608	1.3272
Blue	0.7688	0.7413	0.9772	0	1.0569	0.6835
Cyan	0.8175	1.5022	1.1608	1.0569	0	1.2165
Magenta	0.5340	0.4442	1.3272	0.6835	1.2165	0

Table 4: The center-to-center distance between the six cells given in Table 3.

- |  |  |
|--|--|
| <p>905 [26] M. J. Ward, Spots, traps, and patches: Asymptotic analysis of<br/>906 localized solutions to some linear and nonlinear diffusive sys-<br/>907 tems, <i>Nonlinearity</i> 31 (2018) R189.</p> <p>908 [27] J. H. Merkin, D. J. Needham, S. K. Scott, Oscillatory chemical<br/>909 reactions in closed vessels, <i>Proc. Roy. Soc. London. Series A,</i><br/>910 <i>Mathematical and Physical Sciences</i> 406 (1986) 299–323.</p> <p>911 [28] E. Sel'Kov, Self-oscillations in glycolysis 1. A simple kinetic<br/>912 model, <i>Europ. J. Biochem.</i> 4 (1968) 79–86.</p> <p>913 [29] A. Dhooge, W. Govaerts, Y. A. Kuznetsov, MATCONT: a MAT-<br/>914 LAB package for numerical bifurcation analysis of ODEs, <i>ACM<br/>915 Trans. Math. Soft. (TOMS)</i> 29 (2003) 141–164.</p> <p>916 [30] L. F. Shampine, M. W. Reichelt, The MATLAB ODE suite,<br/>917 <i>SIAM J. Sci. Comput.</i> 18 (1997) 1–22.</p> <p>918 [31] Y. Kuramoto, Self-entrainment of a population of coupled non-<br/>919 linear oscillators, in: International symposium on mathematical<br/>920 problems in theoretical physics, Springer, 1975, pp. 420–422.</p> <p>921 [32] A. Cheviakov, M. J. Ward, Optimizing the principal eigenvalue<br/>922 of the Laplacian in a sphere with interior traps, <i>Math. and Com-<br/>923 put. Model.</i> 53 (2011) 1394–1409.</p> <p>924 [33] R. Straube, M. J. Ward, Intracellular signalling gradients arising<br/>925 from multiple compartments: A matched asymptotic expansion<br/>926 approach, <i>SIAM J. Appl. Math.</i> 70 (2009) 302–332.</p> <p>927 [34] G. Beylkin, L. Monzón, On approximation of functions by ex-<br/>928 ponential sums, <i>Appl. and Comput. Harm. Anal.</i> 19 (2005) 17–<br/>929 48.</p> | <p>930 [35] G. Beylkin, L. Monzón, Approximation by exponential sums<br/>931 revisited, <i>Appl. and Comput. Harm. Anal.</i> 28 (2010) 131–140.</p> <p>932 [36] S. Jiang, L. Greengard, S. Wang, Efficient sum-of-exponentials<br/>933 approximations for the heat kernel and their applications, <i>Adv.<br/>934 Comput. Math.</i> 41 (2015) 529–551.</p> <p>935 [37] M. Pelz, M. J. Ward, Synchronized memory-dependent intracel-<br/>936 lular oscillations for a cell-bulk ode-pde model in <math>\mathbb{R}^2</math>, submitted,<br/>937 <i>SIAM J. Appl. Dyn. Sys.</i> (2024) 50 pages.</p> <p>938 [38] M. A. Henson, D. Müller, M. Reuss, Cell population modelling<br/>939 of yeast glycolytic oscillations, <i>Biochem. J.</i> 368 (2002) 433–<br/>940 446.</p> |
|--|--|